Synthesis, Optimisation, and Characterisation of Rare-earth Analogues of UiO-66

Pedro Rafael Donnarumma

A Thesis

In the Department

of

Chemistry Biochemistry

Presented in Partial Fulfilment of the Requirements

For the Degree of

Master of Science (Chemistry) at

Concordia University

Montreal, Quebec, Canada

June 2021

CONCORDIA UNIVERSITY
School of Graduate Studies

This is to certify that the thesis prepared

By: Pedro Rafael Donnarumma

Entitled: Synthesis, Optimisation, and Characterisation of Rare-earth Analogues of UiO-66

and submitted in partial fulfillment of the requirements for the degree of

       Master of Science (MSc) Chemistry

complies with the regulations of the University and meets the accepted standards with respect to originality and quality.

Signed by the final examining committee:

          Dr. Yves Gélinas   Chair

          Dr. John Capobianco   Examiner

          Dr. Rafik Naccache   Examiner

          Dr. Ashlee Howarth   Thesis Supervisor(s)

                                                      Thesis Supervisor(s)

     Approved by
                   Yves Gélinas, Chair of Department or Graduate Program Director, Faculty of Arts & Science

                   Pascale Sicotte, Dean, Faculty of Arts & Science

Abstract

Title:

Synthesis, Optimisation, and Characterisation of Rare-earth Analogues of UiO-66

Pedro Rafael Donnarumma

This work explores a particular sub-field of metal–organic frameworks (MOFs) incorporating rare-earth (RE) metals, also called RE-MOFs, that have been gaining traction over the last 30 years. The specific family studied here, analogues of the archetypical UiO-66, incorporates RE(III)-hexanuclear clusters and linear organic linkers, giving rise to a network with **fcu** topology named RE-UiO-66. Herein, the following is presented (i) the design, synthesis, and characterisation of the RE-UiO-66 (RE = Y(III), Eu(III), Gd(III), Tb(III), Ho(III), Er(III), Tm(III), and Yb(III)); (ii) the challenges and optimised approaches for the synthesis of each RE-UiO-66 analogue; (iii) the crystalline structure of the entire family of RE-UiO-66 analogues, through the use of single crystal X-ray diffraction (SCXRD); and (iv) the challenges associated with synthesising early lanthanoid analogues of RE-UiO-66 (RE = La(III), Ce(III), Pr(III), and Nd(III)).

Chapter 2 delves into the synthetic optimisation, and characterisation of a series of RE(III) analogues of Zr(IV)-UiO-66. RE-UiO-66 shows several similarities to Zr-UiO-66, a well-studied MOF in the literature; but the post-activation stability of the former is not similar to the latter one, requiring further optimisation. The physical and chemical properties of RE-UiO-66 and some stabilisation pathways, as well as the crystal structure of Tm-UiO-66, are discussed further.

Chapter 3 aims to explain trends in bond lengths observed in the crystal structures of RE-UiO-66 (RE = Y(III), Eu(III), Gd(III), Tb(III), Ho(III), Er(III), Tm(III), and Yb(III)). These trends are then used to explain some of the physical and chemical properties of the RE-UiO-66 series as described in Chapter 2. By using acidic conditions and high temperatures, single crystals suitable for SCXRD are obtained. From this data, the structure of each RE-UiO-66 analogue was solved and refined.

Acknowledgements

First and foremost, I believe none of this work would have been possible if it was not for all the relentless and unconditional support I receive from my wife, Grisel Calcagno. She has been the lighthouse that brought me back every time I wandered away from my goals and objectives, the shoulder upon which I rested my head whenever things looked grim, the peaceful presence that rested next to me while I wrote, studied, or complained about my experiments failing. She sacrificed her time to work in a job away from her field and made this whole experience easier for me, and that is something I will never forget.

Second, I would like to thank my family and friends in Argentina. It has been thanks to the environment they fostered that I am the person I am today. Whenever I felt sad, or I needed to talk they were there for me. Moving to a different country, and leaving everything behind, thousands of kilometres away, is not easy. But somehow, they managed to make me feel like not one centimetre of distance was drawn between us. To my brothers and parents, I owe everything I learned. To my friends, I owe everything I am.

Third, as a researcher I would have been fumbling in the dark constantly if it was not for my supervisor, Dr. Howarth. It was her who introduced me to what I do today. And it was through her natural magnetism that I felt compelled to learn all and everything I could about MOFs. She has listened to all my outlandish and conceptual ramblings and promoted them like only a good supervisor can do. Most importantly, Dr. Howarth made me feel all the time like an equal. To be able to level with your students, make them feel important, and find the time to teach and learn from them is something only an extraordinary person can hope to achieve.

Fourth, I would like to thank all the graduate students with whom I have shared my time while in the Howarth group. Victor Quezada-Novoa and Felix Saraci, next to whom we became the first graduate students ever in the group hold a special place in my heart since we learned everything together. Felix has also helped to pave the road by being our first ever graduate student to finish his degree, many of what he learned through his process was applied in this thesis. I am really proud to be his friend and has truly helped me out in many ways. The amazing Paola Marino, Zvart Ajoyan, Hudson Bicalho, Chris Copeman, and most recently Amna Muhammad and Lars Miller, also contributed to ease my day-to-day research and transformed it into something that

hardly felt like work. I should not forget to mention our adopted member from McGill University, Dr. Hatem Titi, who has taught me so much and always treated me as a really close friend. I could only hope to be like him.

Fifth and last, I want to dedicate a special thanks to all the other laboratory members we have shared space with and the graduate student community at Concordia. On one side, to the undergraduate students I had the pleasure to work with and supervise (particularly, to Valerie Mulvey and Sahara Frojmovic), and also to our sibling group, the Majewski group, without whom the laboratory ambiance would not be the same. On the other side, to every other graduate student from the department of Chemistry, I shall say thank you for being there and just interacting with me in one way or another.

Thanks to all these people, I shall never forget my time as a MSc student at Concordia University.

Contribution of Authors

In all chapters, Dr. Ashlee J. Howarth acted in a supervisory role. Chapters 2 and 3 involved a collaboration with Dr. Hatem M. Titi from the Department of Chemistry at McGill University in Montreal, Canada.

Sections of Chapter 1 have been published as a review: Saraci, F.; Quezada-Novoa, V.; Donnarumma, P. R.; Howarth, A. J. Chem. Soc. Rev. **2020**, 2020, **49**, 7949-7977. I am a primary author of this work. Victor Quezada-Novoa, and Felix Saraci contributed to sections 1.1, 1.2 and 1.6.

A version of Chapter 2 has been published in the form of a communication as: Donnarumma, P. R.; Frojmovic, S.; Marino, P.; Bicalho, H. A.; Titi, H. M.; Howarth, A. J. Chem. Commun. 2021, Advance Article. I am the primary author of this work. Sahara Frojmovic helped in the synthesis and characterisation of Ho-UiO-66 and Gd-UiO-66. Paola Marino performed the ^{1}H-NMR spectroscopy using the basic digestion method. Hudson A. Bicalho performed SEM imaging. Dr. Hatem M. Titi performed SCXRD of Tm-UiO-66, TGA analysis, and VT-PXRD experiments.

Chapter 3 is an advanced project which will soon be made into a manuscript for submission to a peer-reviewed journal. I am the primary author of this work. Sahara Frojmovic has helped with the synthesis of some of the RE-UiO-66 crystals. Dr. Hatem M. Titi has performed SCXRD on some of the RE-UiO-66 single crystals.

Table of Contents

List of Figures

List of Tables

List of Abbreviations

1,4-Benzendicarboxylic Acid	H_2BDC
2,6-Difluorobenzoic Acid	2,6-DFBA
2-Acetamidoterephtalic Acid	BDC-NHAc
2-Benzamidoterephtalic Acid	BDC-NHBz
2-fluoro-4-(1H-tetrazol-5-yl)benzoic Acid	FTZB
Benzoimidephenanthroline Tetracarboxylic Acid	H_4BIPA-TC
Brunauer-Emmett-Teller	BET
Coordination Number	CN
Diffuse Reflectance Infrared Fourier Transform Spectroscopy	DRIFTS
Inductively Coupled Plasma – Mass Spectrometry	ICP-MS
Metal–Organic Framework	MOF
N,N-dimethylacetamide	DMA
N,N-dimethylformamide	DMF
Non-Local Density Functional Theory	NLDFT
Nuclear Magnetic Resonance	NMR
Powder X-Ray Diffraction	PXRD
Rare Earth	RE
Reticular Chemistry Structure Resource	RCSR
Scanning Electron Microscopy	SEM
Secondary Building Unit	SBU
Single Crystal X-Ray Diffraction	SCXRD
Supercritical CO_2	$scCO_2$
Surface Area	SA
Tetrabutylammonium Bromide	TBAB
Thermogravimetric Analysis	TGA
Variable Temperature Powder X-Ray Diffraction	VT-PXRD

Chapter 1

Introduction

1.1. Definition of Metal–Organic Frameworks (MOFs)

The field of MOFs has slowly inserted itself as a giant area of research during the past 30 years. Since the initial works by Hoskins and Robson,[1] followed by pivotal early contributions from Yaghi,[2–4] Kitagawa,[5] and Férey,[6] the systematic discovery and study of scaffolding materials comprised of inorganic and organic building blocks has become a main standard of materials science. MOFs, in particular, have amassed huge attention as potential functional materials.

In principle, MOFs are self-assembled materials formed by the concatenation of inorganic building units through organic building units shown in **Figure 1.1**. The inorganic building units, also known as inorganic nodes, encompass single metal ions, or more complex structures (e.g., chains and clusters), from the s-,[7,8] p-,[9,10] d-,[11–14] and f-block[7,15–17] in the periodic table. Similarly, the organic building units are represented by organic ligands that are capable of linking multiple inorganic units together, regularly called linkers, throughout space. Due to this double flexibility in their composition, MOFs are endowed with a high degree of structure tunability. This, in turn, allows for an attractive programming of characteristics such as porosity, surface area, pore size/shape, density, stability and varying chemical properties.[18] Additionally, and as a result of their structural tunability, MOFs can take shape in 2-, or 3- dimensions, and can be either crystalline or amorphous, with the former being more common.[19,20] This definition overlaps with that of coordination polymers, and indeed, MOFs are a subset of coordination polymers that differ from the rest in that their structure must be open with the potential for voids, or pores.[19,20]

MOFs are known for presenting remarkable permanent porosity, with some examples displaying up to 90% free volume,[21] surface areas reaching 7,800 m^2/g,[22,23] and densities as low as 0.124 g/cm^3,[24] values that distinguish MOFs from related materials like zeolites and 1-D coordination polymers.[22,25,26] Due to their previously mentioned properties, MOFs have proven to be potentially useful in various applications, including but not limited to, gas adsorption,[27–29] catalysis,[11,30–32] chemical sensing,[33,34] and water treatment.[35–37]
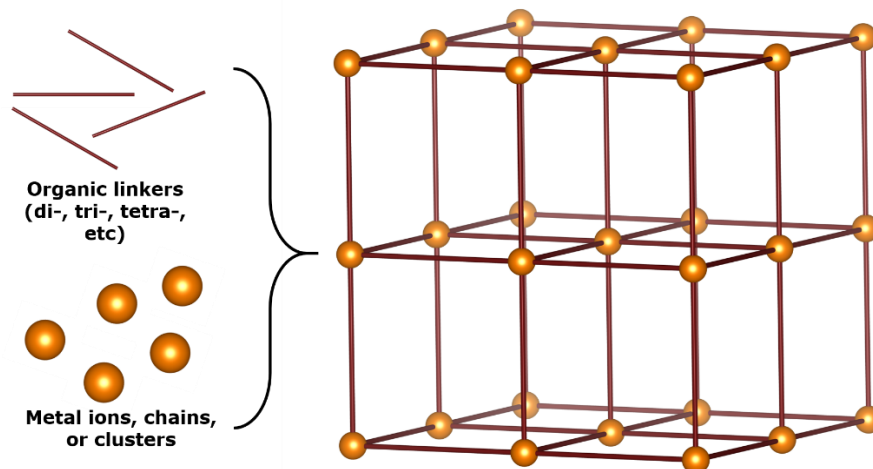
Figure 1.1. Schematic representation of a MOF structure assembling.

1.2. Rare-earth Metal–Organic Frameworks (RE-MOFs)

As with any other family of materials, MOFs can be divided into subsets in accordance with different criteria. One of these criteria involves classifying them according to the metal forming the inorganic nodes. A subset of MOFs that are of interest from both a fundamental synthetic, and application standpoint are those assembled using rare-earth (RE) metal nodes.[38–40] Yttrium, scandium, and the series of fifteen lanthanoids are included (**Figure 1.2**) in the RE-metal denomination. The reason behind this terminology is that yttrium and scandium are chemically similar to the lanthanoids, and studies in literature involving the late lanthanoids often include yttrium and scandium. What is interesting about these elements is their coordination chemistry, which is very diverse, with small energetic differences between different coordination numbers and geometries, and where geometries are primarily dictated by ligand steric effects.[41] The variability of RE-metals results in more complicated structure prediction and synthesis, but it opens the way for the discovery of several new structures, comprised of diverse metal nodes, sometimes with highly connected nets, and with the possibility of merging multiple net structures using only one metal.[42,43] In opposition to the *d*-block metals, the *f*-block metals have unique electronic properties dictated by their 4*f* electron configurations.[44] Given that the 4*f* orbitals are shielded from the external environment by the 5*s* and 5*p* orbitals, the lanthanoid metals have distinct electronic, and magnetic properties that are scarcely affected by coordinating ligands.[44]

So, by carefully tuning the RE-metal node and organic linker components, RE-MOFs can be assembled into fascinating structures with diverse and complex topologies, presenting endless possibilities for the development of functional materials.

Figure 1.2. RE elements highlighted on the periodic table.

1.3. Directing Principles for MOF Design and Synthesis

1.3.1. Reticular Chemistry

Yaghi and O'Keeffe introduced reticular chemistry as the foundation of MOF synthesis in which the formation of ordered network materials is established through the coming together of predetermined net structures.[45–47] What this means is that by understanding the geometry and the connectivity of the building blocks that make up a net, there is the possibility of building the same net with several other building blocks that present similar (or the same) geometrical characteristics and connectivity.[48] In the MOF field these building blocks are the inorganic nodes and the organic linkers which coalesce into what is known as secondary building units (SBUs) to assemble a MOF.

1.3.2. Topology

As a system becomes more complex, a procedure becomes necessary to describe it and distinguish it from other closely related systems. For example, in organic chemistry when an alkene is described it is important to denote whether it is the *E*, or the *Z* stereoisomer. The same is true with networks of such complexity as in MOFs, wherein a 4-connected net can be represented by multiple descriptors. These representative nets in the field of MOF chemistry are known as topologies, a mathematical construct describing the connectivity of nets which are represented by a bolded three-letter code and collected in the Reticular Chemistry Structure Resource (RCSR).[48]

In the case of a 4-connected net, it could be found that this net has a diamond (**dia**), quartz (**qtz**) (**Figure 1.3**), or another topology. Describing MOFs by their net structure is thus necessary to fully understand the underlying connectivity and make comparisons among different materials. An important thing to note is that topologies are indifferent to bending, stretching, and squeezing,[49] but not to bond breaking. Although there is an infinite number of topologies, only a handful of them occur with regularity and these can be found in the RCSR.[49]
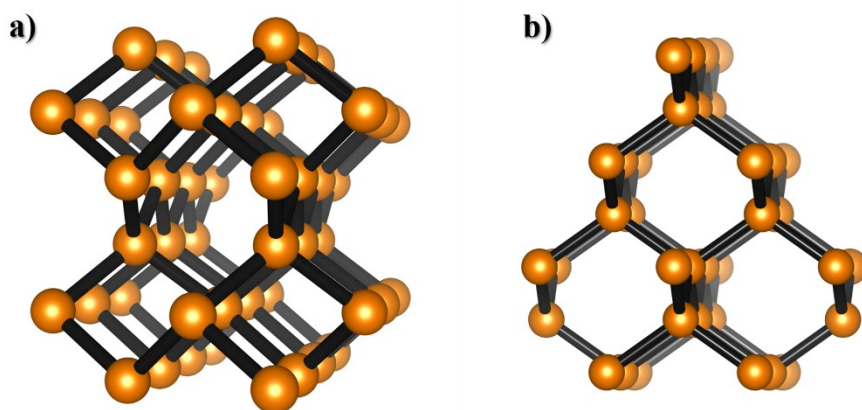
Figure 1.3. Representation of two 4-connected nets; (a) the chiral **qtz** net, and (b) the achiral **dia** net.

An advantage of the existence of the use of topologies to describe the underlying MOF nets is that it leads to i) understanding the structure of the prepared material; ii) better comparison to materials others have made; iii) more efficient scientific communication within the field; iv) the design of new materials through the reticular chemistry scheme.

1.4. Archetypical MOFs and UiO-66

1.4.1. What is an Archetypical MOF?

Currently, when searching "metal organic framework" in SciFinder, there are more than 20,000 hits returned. However, this is not a synonym of the plurality of MOF structures since most of the research done focuses on only a handful of MOFs. So, in accordance with Mu *et al.*,[50] an archetypical MOF is defined as a MOF studied or discussed in more than 1,000 publications. Then,

the number of archetypical MOFs is found to be six, in order: ZIF-8, MIL-101, UiO-66, MOF-5, HKUST-1, and MIL-53.[50]

1.4.2. Zr-UiO-66

From all the previously mentioned archetypical MOFs, the work herein involves the UiO-66 platform. First reported in 2009 by the Lillerud group,[51] it was synthesised and discovered at the University of Oslo, giving the name UiO. Over the years this MOF has garnered significant attention, leading to an exponential increase in the number of publications on this material (**Figure 1.4**).

UiO-66 is easy to synthesise at lab-scale and is a crystalline MOF with high relative stability, and several potential applications. UiO-66 is generally synthesised solvothermally from 1,4-benzencedicarboxylic acid (H$_2$BDC) and different Zr(IV) salts from which a polynuclear cluster forms (**Figure 1.5a**), primarily in DMF.[51–53] Other additives, called modulators, can be added to the reaction mixture to vary some of the structural properties of the material such as defectiveness, crystallinity, or crystal size.[54,55] From now on, UiO-66 will be referenced as Zr-UiO-66 to differentiate it from other similar structures.
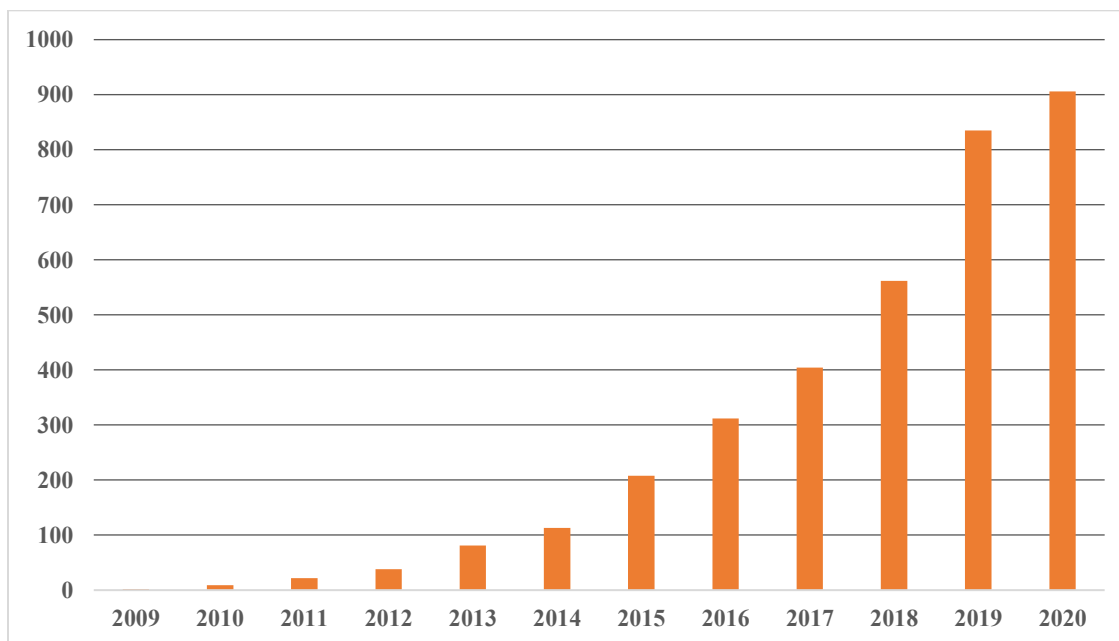
Figure 1.4. Number of hits/year returned in SciFinder for keyword "UiO-66". Does not include patents.

In its most stable form, also known as the hydroxylated form, Zr-UiO-66 has a face-centred-cubic unit cell with the space group *Fm-3m* (**Figure 1.5b**), and a lattice parameter, a, of 20.7 Å.[51] It contains two distinct types of cages, an octahedral one of 12 Å diameter (**Figure 1.5c**) and 6 Å aperture, and a tetrahedral cage of 7.5 Å (**Figure 1.5d**).[56] As a result of this, the calculated theoretical pore volume of Zr-UiO-66 is 0.77 cm^3/g, and its surface area is 1,160 m^2/g.[57,58]

According to the RCSR classification system for topologies, Zr-UiO-66 has an **fcu** topology, which is described also as having a connectivity of 12.[45] The 12-connected node of the net comes from the inorganic building block comprised of the Zr(IV)-hexanuclear cluster, which is bridged to 12 other clusters through BDC linkers.[18] In this hexanuclear cluster, each bridging hydroxide (or oxide) links three Zr(IV) ions. It is the high connectivity of this building block, and the strength of the Zr(IV)-O bond that determines the high stability of this material.

1.4.3. Zr-UiO-66 Isoreticular Structures

Perhaps one of the most attractive aspects of Zr-UiO-66 is the broad range of materials to which it opens the doors to without profound changes in the synthetic procedures. Isoreticular structures are said to have the same topology, but their building units might change (Section 1.3.2). Isoreticular UiO-66 structures have been reported using different tetravalent metals — Zr(IV),[52] Hf(IV),[59] Ce(IV),[60] Th(IV),[61] U(IV),[62] Pu(IV)[63] with H$_2$BDC.[59–63]
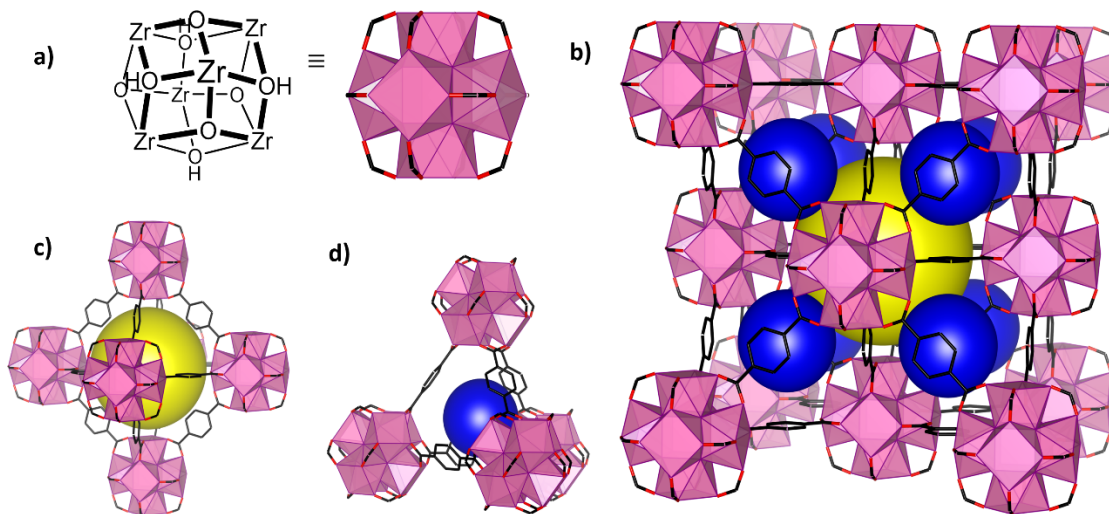
Figure 1.5. Scheme of Zr-UiO-66 structure showing (a) the Zr$_6$-cluster structure, (b) the **fcu** structure, (c) the octahedral cage, and (d) the tetrahedral cage.

1.4.4. RE-Metal Cluster Nodes for RE-UiO-66 Isoreticular Structures

Over the years, research efforts have been focused on the synthesis and isolation of discrete, polynuclear RE-oxo/hydroxo clusters.[64–66] It has been found that controlled hydrolysis of the RE precursors is needed in order to ensure the formation of discrete clusters over much preferred RE chains, oxides, and hydroxides in the presence of carboxylic acid ligands. An easy way to achieve controlled hydrolysis is through the regulated addition of base to a water/ethanol solution to drive the formation of a RE-based hexanuclear complex.[67] Controlled hydrolysis can also be achieved by using ligands acting as directing agents and stabilising capping groups to form discrete clusters that can, afterwards, be used as precursors under specific conditions.[64,68] Similarly, the same clusters can be generated and stabilised during the synthesis of RE-MOFs. The nuclearity of these clusters can vary from 2 to 9, as in the case of Y-CU-10,[69] or even values as high as 26 are reported.[70]

The potential of RE(III)-hexanuclear clusters to be used as SBUs in MOFs was shown by Yao *et al.* in 2008.[71] In this example, the octahedral unit $[Er_6(\mu_6\text{-O})(\mu_3\text{-OH})_8]^{8+}$ is repeated in one direction to achieve a rod shaped structure, giving a hybrid between a RE(III)-chain and RE(III)-cluster node. More recently, Eddaoudi *et al.* reported a series of RE(III)-MOFs with **fcu** topology,[15] after recognising the similarities between the RE(III)-hexanuclear cluster and the Zr(IV)-hexanuclear cluster already known to be used in MOF synthesis since 2009.[51] It was found in this work that in order to build the hexanuclear cluster *in-situ*, the aid of a fluorinated linker (or modulator) was required under regular MOF synthesis conditions. For example, using 2-fluoro-4-(1H-tetrazol-5-yl)benzoic acid (FTZB) as a linker, the metal cluster $[RE_6(\mu_3\text{-OH})_8(O_2C-)_6(N_4C-)_6]^{2-}$ (RE = Y(III) and Tb(III)) is generated and serves as a 12-connected node, leading to the first RE(III)-MOFs with **fcu** topology (**Figure 1.6a**).[15] Particularly, in examples where non-fluorinated linkers were used, a fluorinated modulator was required (**Figure 1.6b**).[43,69] Other studies have shown that other fluorinated modulators, such as 2,6-difluorobenzoic acid drive the formation of the RE cluster, and therefore RE-MOFs.[72]

Since then, multiple RE(III)-based isoreticular UiO-66 (RE-UiO-66) structures have appeared in the literature containing different functionalised BDC linkers.[29,72–74] Curiously, until now, there was no example in the literature of a RE-UiO-66 analogue synthesised using non-functionalised BDC linkers.
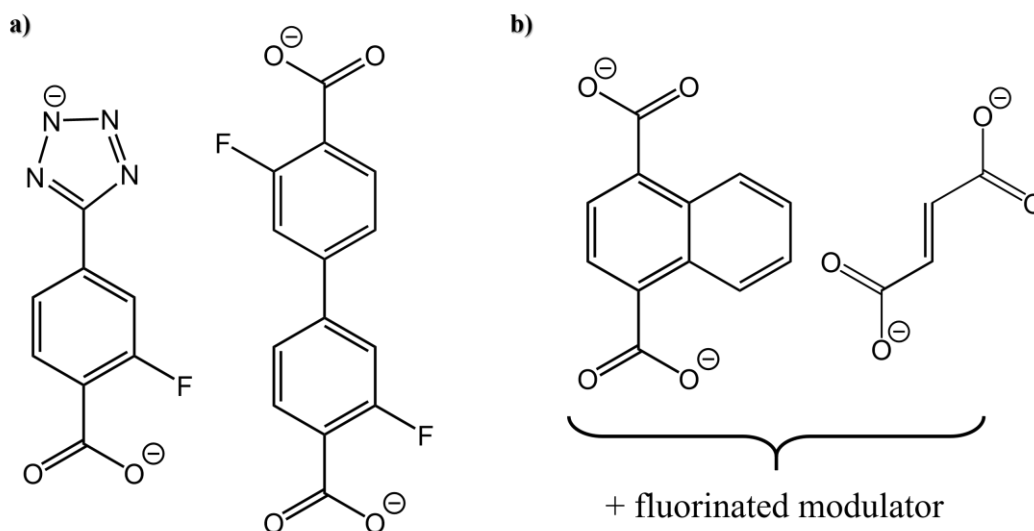
Figure 1.6. Structure of some of the first linkers used in the synthesis of **fcu** RE-MOFs, note that fluorine is present in either (a) linker, or (b) modulator.

1.5. Overview of Methods in MOF Synthesis

1.5.1. MOF Synthesis

There are several methods that can be used to synthesise MOFs.[75] As a general rule, synthesis conditions are chosen to allow the metal-ligand bonds to be broken and reformed thus leading to structure propagation. Solvothermal synthesis is the most straightforward and commonly used method.[75] Simply, it entails the mixing of a metal salt with an organic linker in a solvent (generally with a high boiling point) inside a vessel. The mixture is then heated either in an oven or on a hotplate for different amounts of time. From there, different parameters can be systematically optimised to ensure the formation of the desired product with a determined topology, purity, and other physical characteristics such as particle size.[76–78]

Moreover, in some instances the use of a modulator might be necessary to help prevent rapid precipitation or to direct a reaction towards the formation of a product otherwise very difficult to obtain.[15,79,80] Modulators are non-structural, monotopic ligands which can form dynamic bonds with the metal precursor and help to slow down the formation of structural bonds by competing with the linker for metal coordination sites.

Alternative MOF synthetic strategies include electrochemical,[81,82] mechanochemical,[83,84] sonochemical,[85] and microwave-assisted synthesis,[85] among others.

1.5.2. MOF Activation

Due to the porous nature of MOFs, it is inevitable that during solvothermal synthesis some of the solvent molecules will be trapped inside the pores of the framework (**Figure 1.7**). In order to access freely the voids in MOFs, it is necessary to remove these guest molecules — a process called activation. Activation processes are also diverse in nature, with i) vacuum drying being the most common one,[86–88] in addition to, ii) supercritical CO_2 (scCO$_2$) drying,[89,90] iii) freeze drying,[91,92] iv) chemical treatment,[12,93] or microwave activation.[94,95]

As synthesised   **Dried**   **Activated**
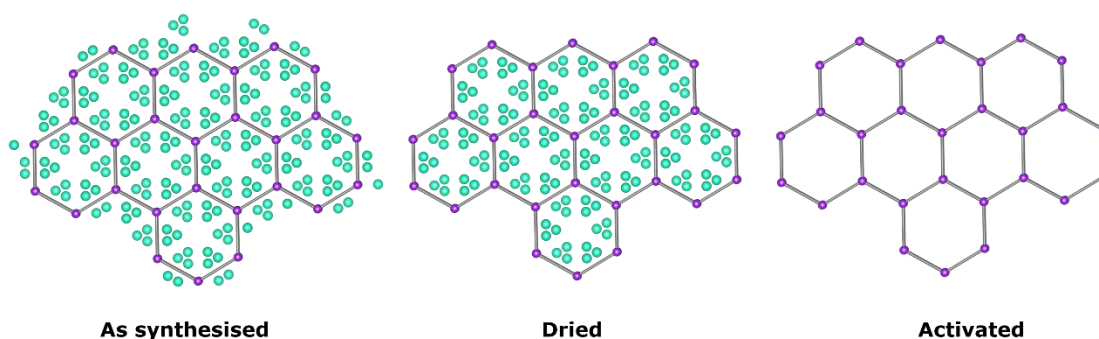
Figure 1.7. Representation of an as-synthesised MOF (left), a dried MOF (centre), and an activated MOF (right). The light-blue spheres represent trapped molecules.

1.5.2.1. Solvent-Exchange Activation

Maintaining the structural integrity of a framework is key to accessing the highest possible surface area of a MOF. When the synthesis of a MOF involves a high boiling point solvent (i.e., DMF, water) with elevated surface tension, strong capillary forces may be produced by the solvent and direct heating activation might lead to collapse of the structure.[96–98] To avoid this situation, one of the most common ways of proceeding involves the exchange of a high boiling point solvent for a lower-boiling-point/lower-surface-tension solvent (i.e., acetone, methanol) before heating the sample under vacuum.[86–88,91]

A typical solvent exchange follows a simple procedure. First, the sample is washed multiple times with the synthesis solvent to ensure the removal of non-solvent guest molecules

(i.e., non-coordinated linker, modulator). In this, the material is soaked for some time between each wash, allowing for a final overnight wash. Then, the procedure is repeated but this time with the low boiling point solvent which will replace the high boiling point solvent upon infiltration in the structure. This procedure might be optimised (for example, by allowing for longer soaking times) to guarantee the maximum removal of all the guest molecules.

1.5.2.2. scCO$_2$ Activation (Supercritical Drying)

A milder activation technique, which falls under the solvent exchange category, is termed supercritical carbon dioxide (scCO$_2$) activation.[91] The advantage of using this technique over conventional solvent exchange is related to the fact that it avoids the liquid to gas-phase transformation of the guest solvent by going through a supercritical phase, eliminating the effects of surface tension and capillary forces.[91] Due to the higher complexity of this technique and the need for specialised equipment, it is more frequently used when conventional solvent exchange causes framework collapse.

Similar to conventional solvent exchange, scCO$_2$ drying involves various solvent exchange steps. Initially, the MOF is exchanged with a solvent that is miscible with liquid CO$_2$, such as ethanol, and soaked overnight. The material is then placed in the scCO$_2$ dryer and cooled down to temperatures between 2-10 °C after which multiple solvent exchanges with liquid CO$_2$ occur. The final step involves heating the system to the supercritical temperature and pressure of CO$_2$, and then slow release of the scCO$_2$ slowly from the MOF.

1.5.3. Characterisation of MOFs

The most elemental MOF characterisation methods include powder X-ray diffraction (PXRD), to establish the crystallinity and phase purity of the material, and nitrogen (N$_2$) adsorption/desorption isotherms, to assess porosity and calculate the apparent surface area of the material.[75] Additionally, other characterisation techniques can describe further the structure and properties of MOFs, these include i) single crystal X-ray diffraction (SCXRD), to obtain absolute structural information; ii) thermogravimetric analysis (TGA), to assay the thermal stability of the MOF; iii) scanning electron microscopy (SEM), to study the morphology and size of the crystals; iv) NMR spectroscopy, to study the nature and ratios of linkers, modulators, and other guest molecules inside the pores; and v) diffuse reflectance infrared Fourier transform spectroscopy

(DRIFTS); and vi) inductively coupled plasma – mass spectrometry (ICP-MS), to probe the percentage of metal, or study metal ratios in a MOF. A more detailed discussion of these techniques applied to MOFs is exposed below.

1.5.3.1. Powder X-Ray Diffraction (PXRD)

In the field of MOFs, PXRD is one of the two most important techniques since it allows for the collection of information about bulk crystallinity. Moreover, once the diffractogram is obtained, and the sample is determined to be crystalline, other information can be extracted from it (e.g., phase composition, crystallite size, unit cell dimensions). Most importantly, phase purity can be corroborated through comparison of the obtained patterns with a simulated one which can be generated from single-crystal data (**Figure 1.8**) or other types of modelling.[98]
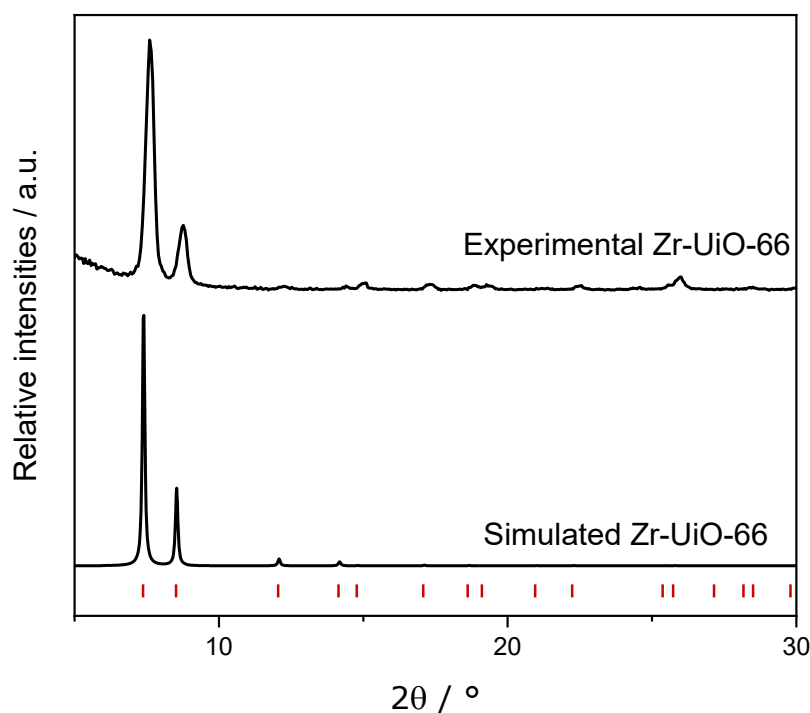
Figure 1.8. Stacked PXRD patterns exemplifying a comparison between an experimentally obtained one (top), and a simulated one (bottom). The red tick marks are the allowed reflections.

Typically, a PXRD experiment involves loading a powdered sample onto a sample holder *via* dry loading or transference using a volatile solvent or oil.

Often, there are variations between the simulated PXRD pattern of a MOF and its experimental counterpart, which can be attributed to different factors including:

- Preferred orientation: If a crystal morphology is that of plates or needles, then upon loading on the flat sample holder the crystals may pack with a preferred orientation. As a result, the intensity ratios in the diffractogram are modified. This problem can often be circumvented through sample rotation.[99]

- Broad diffraction peaks: This phenomenon is commonly associated with having small crystallites, which in turn leads to Scherrer broadening.[100,101]

PXRD is crucial in the process of designing and synthesising new MOFs through reticular chemistry, as it allows for comparison of a known isoreticular structure pattern with the newly synthesised MOF. If there is a match between these two, then it can be established that both structures have the same topology.

1.5.3.2. Single Crystal X-Ray Diffraction (SCXRD)

When a single crystal of a MOF is available, single crystal X-ray diffraction (SCXRD) becomes the most reliable proof of its structure.[102] SCXRD is used to unambiguously determine the position of the atoms that give rise to the framework itself. But its utility can go beyond that, having been used as evidence of other important features of MOFs — e.g., position of main adsorption sites,[101] proof of post-synthetic modification success,[103,104] and precise identification of pore-occupying species.[105] The main challenge is to grow a MOF of appropriate crystal size (> 50 μm) and quality.[75] In order to make it, minute control over the synthesis conditions must be exerted so as to favour these two points.

Even after obtaining a suitable crystal for SCXRD, the characteristic low density of MOFs presents two features which can make structure determination a challenge, i) the presence of pore-occupying species, and ii) high possibilities of crystal twinning due to their high symmetry.[102] Of these two, only the first one is of importance for this work.

Upon a crystal structure determination, the experimentally measured intensities of each reflection are corrected for several factors to obtain what is known as the structure factor (F_{obs}) for each reflection. Crystal structure determination is performed through modelling of the structure which involves calculation of F_{calc}, which is compared directly against F_{obs}. The relative error between them is what constitutes the crystallographic R-factor:

$$R = \frac{\sum_{hkl}|F_{obs}-F_{calc}|}{\sum_{hkl}|F_{obs}|} \quad \textbf{(Equation 1.1)}$$

According to **Equation 1.1**, an R-factor value of 0 represents perfect agreement between model and measurement. It is considered that an R < 5% denotes a structure model of high quality, with higher numbers representing increasingly worse solutions.[102]

Similarly, a second factor, R_{int}, is used as a measure of the deviation of equivalent reflections in the chosen space group (**Equation 1.2**) — e.g., (200), (020), and (002) in a cubic structure.

$$R_{int} = \frac{\sum_{hkl}|F_{obs}^2 - \overline{F_{obs}}^2|}{\sum_{hkl}|F_{obs}^2|} \quad \textbf{(Equation 1.2)}$$

Theoretically, the structure factors of equivalent reflections have the same value. So, if the value of R_{int} > 10%, this can be considered a sign of systematic error, commonly that the structure has been solved in the wrong Laue class. Another reason for this factor to be high is related to the signal-to-noise ratio.

Since low-density compounds, such as porous MOFs, can contain voids up to 90% of the unit cell volume,[21] this space tends to be filled with guest molecules (generally the solvent).[106] It is known that if left inside the pores, these molecules can have a large effect on diffraction.[4,53] It has been reported that the intensities of the low-angle reflections in PXRD are affected by solvent loading in the sample.[107,108] Coincidentally, low-angle reflections tend to have higher intensities in a pattern due to exponential decay in the atomic X-ray scattering factor. Seeing how the most intense reflections are also the most affected by the contents of the pores, it is important to correctly model these contents.[102]

Because the solvent in the pores tends to be highly disordered, it is extremely difficult to model correctly, especially in MOF crystal structures which tend to be of high symmetry.[102] A very common technique used to improve the rigid part (crystalline part) of MOF crystal structures is called solvent masking.[109] If the correct structure has been modelled for the rigid part, a solvent masking program can be used to calculate the scattering contribution of the disordered species in

the pores to the structure factor and remove them altogether. The most commonly used solvent masking program is SQUEEZE.[109] Notwithstanding the popularity and effectiveness of this technique to "improve" the quality of the model in the MOF literature, its use must be restricted to structures with data that:[102]

- has been determined to be in the right space group with any twinning resolved.
- has high quality and completeness, paying special attention to the intensity of the low-angle reflections.

1.5.3.3. Nitrogen (N_2) Adsorption/Desorption

Gas adsorption/desorption isotherms can be used to probe apparent surface areas, pore volumes, and pore size distributions. Most commonly in the MOF field, N_2 gas at 77 K is used as the standard adsorbate for surface area and pore size analysis.[75] Before running a N_2 isotherm measurement, the sample should be appropriately activated to obtain representative data. An isotherm can be classified under six different types, with some of them presenting subtypes, according to the present pore size in the material.[110,111] First, pore sizes (d) are classified as i) micropores (d < 2 nm); ii) mesopores (2 nm < d < 50 nm); and iii) macropores (d > 50 nm). Based on their shape (**Figure 1.9**), isotherms are classified as: i) Type I, given by microporous solids and subcategorised in Type I(a) — given by materials with narrow micropores (d < 1 nm) — and Type I(b) — with larger micropores —; ii) Type II and III, in which the material is non-porous or presents macropores, with the difference that the second one does not present an identifiable gas monolayer formation; iii) Type IV, observed in mesoporous materials with capillary condensation, and that can be further subcategorised into Type IV(a) — materials with cylindrical pores bigger than 4 nm —, and Type IV(b) — with mesopores smaller than 4 nm —; iv) Type V, similar to Type III but with pore filling happening at a higher relative pressure; and v) Type VI, given by nonporous materials which present a uniform layer-by-layer deposition.

After obtaining the N_2 isotherm, a careful analysis must be performed since surface areas can be easily over or underestimated.[112,113] As of today, the default practice is to use Brunauer-Emmett-Teller (BET) theory since it describes the existence of multilayer gas adsorption,[114] more in tune with what happens in reality during physisorption processes in a MOF. In contrast to this, the Langmuir theory allows for the existence of only a gas monolayer which leads to overestimation of the surface area of many MOFs.[115] Similarly, pore size distribution can also be

obtained from analysis of the collected N_2 isotherm,[75] and the most accepted model used is non-local density functional theory (NLDFT),[116,117] as it is able to accurately fit isotherm data corresponding to mesopores and micropores.
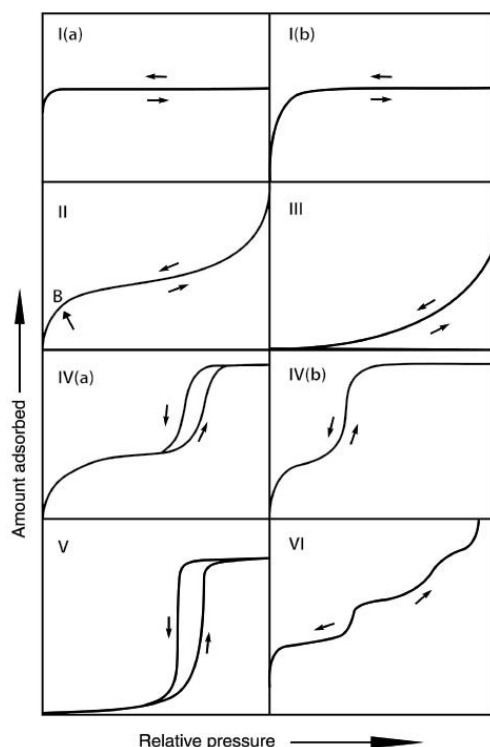
Figure 1.9. Different isotherm shapes found in porous and non-porous materials. Figure obtained from Thommes *et al*.[110]

1.5.3.4. Thermogravimetric Analysis (TGA)

Thermogravimetric analysis (TGA) is a technique used to partly analyse the thermal stability of a MOF, as well as to determine the weight percentage corresponding to solvent, linker, and the inorganic portion of the material. A TGA alone is not enough to study the stability of a MOF since the material can undergo a phase transition without having to lose mass. Then, using a complementary methodology such as variable temperature PXRD (VT-PXRD) can help discern whether the MOF remains stable and in the same phase as temperature raises.[118,119] If used appropriately, TGA can help with determining the correct molecular formula of the MOF, e.g. when the experimental MOF structure deviates from its ideal structure because of defects.[75,120]

1.5.3.5. Scanning Electron Microscopy (SEM)

Scanning electron microscopy (SEM) is useful to measure different MOF properties including crystal size, morphology, and elemental composition if coupled to an energy-dispersive X-ray spectroscopy detector.[75] Because the acceleration voltage of the electron beam can induce phase transitions, or overall, degradation, MOF samples are sometimes coated with a conducting material that helps decrease the charge build up generated by the electron gun. **Figure 1.10** shows an SEM image of Y-CU-10 synthesised for the first time in 2019.[69]
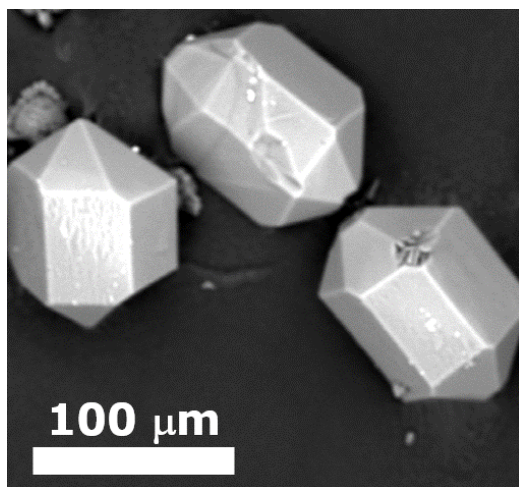
Figure 1.10. SEM micrograph of MOF Y-CU-10.

1.5.3.6. NMR Spectroscopy

Nuclear magnetic resonance (NMR) spectroscopy can be used to determine MOF purity, linker incorporation, and modulator and solvent presence in the material. MOFs are not soluble in conventional NMR solvents and therefore must be digested in order to obtain a spectrum. Regularly, acid digestions are performed on a MOF,[121] in which a mass (~1-3 mg) of the material is treated with a few drops of a deuterated acid (e.g., D_2SO_4, DCl) and sonicated or heated before adding a solvent capable of dissolving the components of the MOF (e.g., DMSO-d_6). Alternatively, a basic digestion can be performed on the MOF as well.[75] **Figure 1.11** is an example of a ^{1}H-NMR spectrum obtained from an acid digestion of Zr-UiO-66.
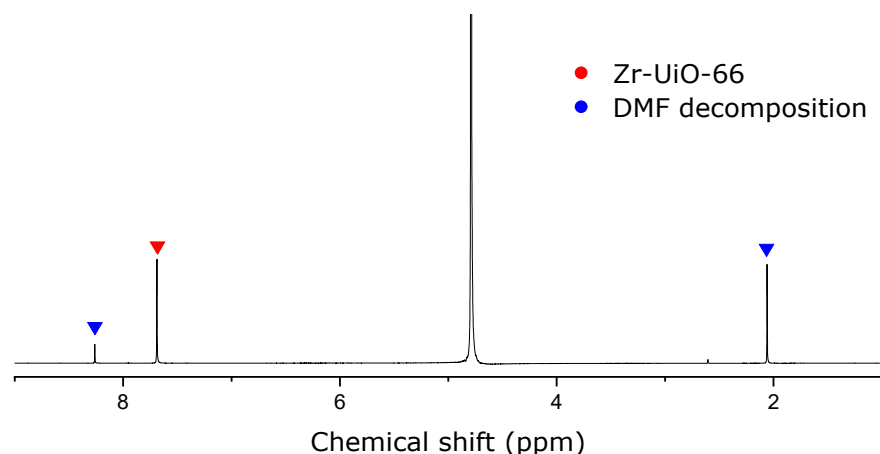
Figure 1.11. ^{1}H-NMR spectrum of Zr-UiO-66 showing the BDC aromatic H (red) and DMF decomposition products, dimethylamine — near 2 ppm —, and formate — near 8 ppm — (blue).

1.5.3.7. Inductively Coupled Plasma Mass Spectrometry (ICP-MS)

Inductively Coupled Plasma Mass Spectrometry (ICP-MS) can be used to confirm purity or elemental ratios in a MOF.[75] As with NMR spectroscopy, the sample must be digested before being measured in an ICP-MS experiment. The most common digestion methodologies use acid matrices, such as HNO_3 or H_2SO_4, in pair with a heating method (microwave assisted digestion or conventional heating). ICP-MS gives information about the concentration of an element in the digested solution, which can be directly associated with the molecular formula of a MOF.

1.5.3.8. Diffuse Reflectance Infrared Fourier Transform Spectroscopy (DRIFTS)

DRIFTS is generally used to determine the presence and identity of IR-active species in MOFs since it is a technique designed for powder samples (**Figure 1.12**). In order to optimise the signal for the experiment, the MOF is diluted in an IR-transparent matrix such as KBr. Usually, this is performed by gently grinding the MOF together with KBr using a mortar and pestle to ensure homogeneity of the sample. Characteristic IR bands observed in MOFs include C=O, O-H, and C-H stretching recurrently found on organic linkers. Conversely, the IR bands observed are not only limited to the organic portion of MOF. For example, O-H stretching coming from the inorganic building units can be observed in Zr-UiO-66 (Figure 1.12).[50] Because signals from H_2O

17

can be very intense, it is important that both the sample and the KBr remain dry when performing this experiment.[75]
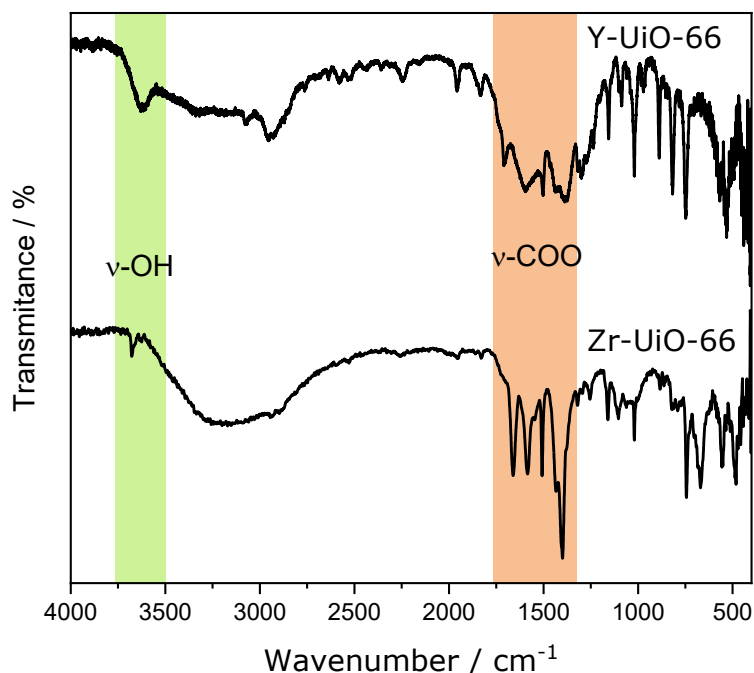
Figure 1.12. DRIFTS spectra of Zr-, and Y-UiO-66 from this work.

1.6. Potential Applications of MOFs

As previously mentioned, MOFs have an interesting set of properties which makes them potentially excellent candidates for a wide range of applications including, but not limited to, sensing,[33,34] gas adsorption,[27–29] chemical separations, catalysis,[11,30–32] drug delivery,[122,123] near infrared emission,[124–126] proton conductivity,[127] and single molecule magnets.[128] Research in some of these areas have taken MOFs into commercial applications. In concrete, the first commercial applications of MOFs were unveiled in 2016 by NuMat Technologies,[129] and MOF Technologies.[130] Although, none of these applications are exclusive to RE-MOFs, there are examples that do take advantage of the unique properties of RE metals (primarily lanthanoids). Some examples of potential applications are presented to focus on the use of RE-MOFs for their Lewis acid characteristics in catalysis.

1.6.1. RE-MOFs for Catalysis

RE-compounds have appealing Lewis acid characteristics, making them attractive as potential catalysts for a wide variety of transformations.[131] While several RE compounds can be used as homogeneous catalysts,[132–135] there are added advantages to designing stable, solid materials that can be used as heterogeneous catalysts such as reusability and recovery of the catalyst.[136] MOFs are exceptional candidates for heterogeneous catalysis.[30,137] MOF metal nodes can be tuned to have varying numbers of accessible Lewis acidic sites, while the organic linkers can be used to i) tune pore size and shape for diffusion, ii) introduce functional groups that may help with substrate-catalyst interactions, and/or iii) present additional catalytic sites for tandem catalysis. RE-MOFs are of interest for many of the same reasons as other MOF families, while the high variation and tunability in coordination number and modes of RE(III)-ions makes RE-MOFs a particularly diverse family of catalysts. In recent years, various studies have been conducted pertaining to the use of RE-MOFs as heterogeneous catalysts for organic reactions and some examples will be discussed.

One potential catalytic application of MOFs,[138] including RE-MOFs, involves using waste CO_2 as a reactant, by adsorbing it and subsequently transforming it into finer chemicals. In recent years, a handful of examples have been reported studying RE-MOFs as catalysts for this purpose.[139–142]

In one example, Gándara, Nguyen *et al.* synthesised a series of RE-MOFs (RE = Nd(III), Eu(III), and Tb(III)) comprised of benzoimidephenanthroline tetracarboxylic acid (H_4BIPA-TC) linkers and RE(III)-chain nodes to give MOF-590, -591 and -592.[140] In their study, the oxidative carboxylation of styrene using CO_2 was examined using the RE-MOFs as catalysts. Although the entire series revealed promising catalytic activity when using co-catalysts, tetrabutylammonium bromide (TBAB), and anhydrous tert-butyl hydroperoxide, MOF-590 (**Figure 1.13**) comprised of Nd(III)-nodes, demonstrated the best performance under mild conditions. Using MOF-590 as a catalyst, 93% of styrene was converted to product with 94% selectivity and 87% yield of styrene carbonate after 10 h at 80 °C under 1 atm of CO_2. The reaction was performed in the absence of solvent, and with a MOF catalyst loading of 0.18 mol%. The catalytic activity in all cases was attributed to the RE-MOFs having a large number of coordinated H_2O molecules that can be removed to yield accessible Lewis acid sites.

Another class of reactions that can be catalysed by RE-MOFs are those involving the formation of C–C bonds, which can occur through many different paths with varying substrates.[143–147] Pombeiro *et al.* reported five RE-MOFs (RE = La(III), Ce(III), Sm(III)) comprised of trinuclear RE(III)-cluster nodes and 2-acetamidoterephtalic acid (BDC-NHAc) or 2-benzamidoterephtalic acid (BDC-NHBz) linkers.[146] The MOFs were studied as catalysts for the conversion of various benzaldehyde substrates in the presence of nitroethane and water, to give the corresponding β-nitroalkanol (**Figure 1.14**). The Sm-BDC-NHAc MOF performed the best as a catalyst for this Henry reaction, producing optimised yields near 70% in all cases with a catalyst loading of 3.0 mol%. The superior catalytic activity of the Sm(III) derivative was attributed to the higher Lewis acidity of Sm(III) vs. Ce(III) and La(III).
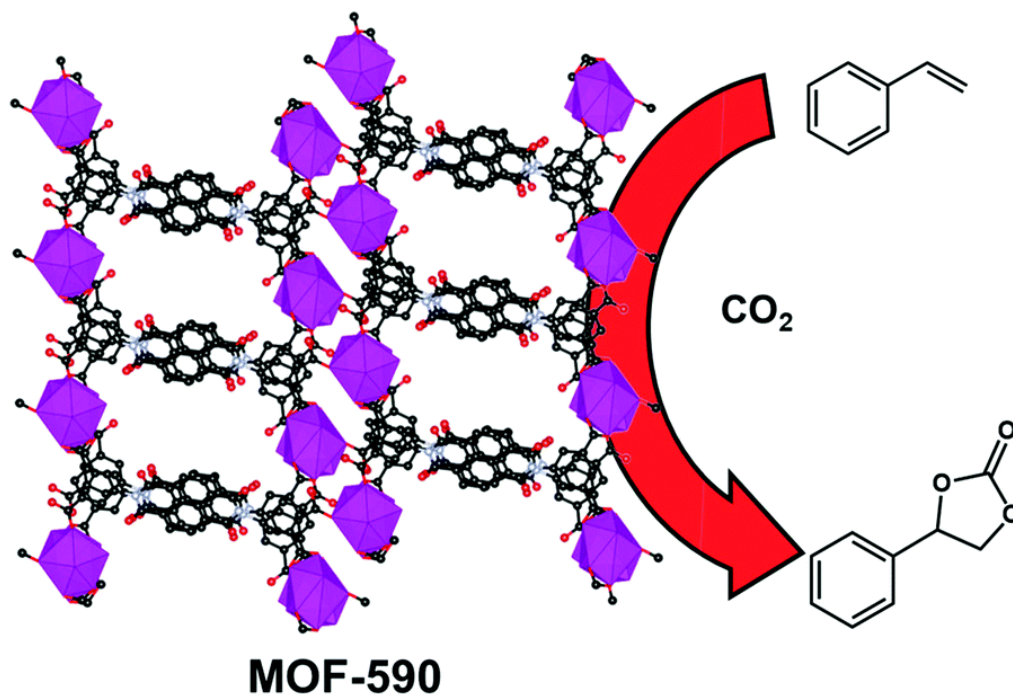
MOF-590

Figure 1.13. Oxidative carboxylation of styrene using CO_2 catalysed by MOF-590. Nd = purple, C = black, O = red, N = light blue. Hydrogen atoms omitted for clarity.

Although some examples of reactions that can be catalysed by RE-MOFs have been highlighted here, the list is not exhaustive. RE-MOFs have also been studied as catalysts in oxidation,[148–150] polymerisation,[151] and condensation reactions,[152] and as catalyst supports.[153]
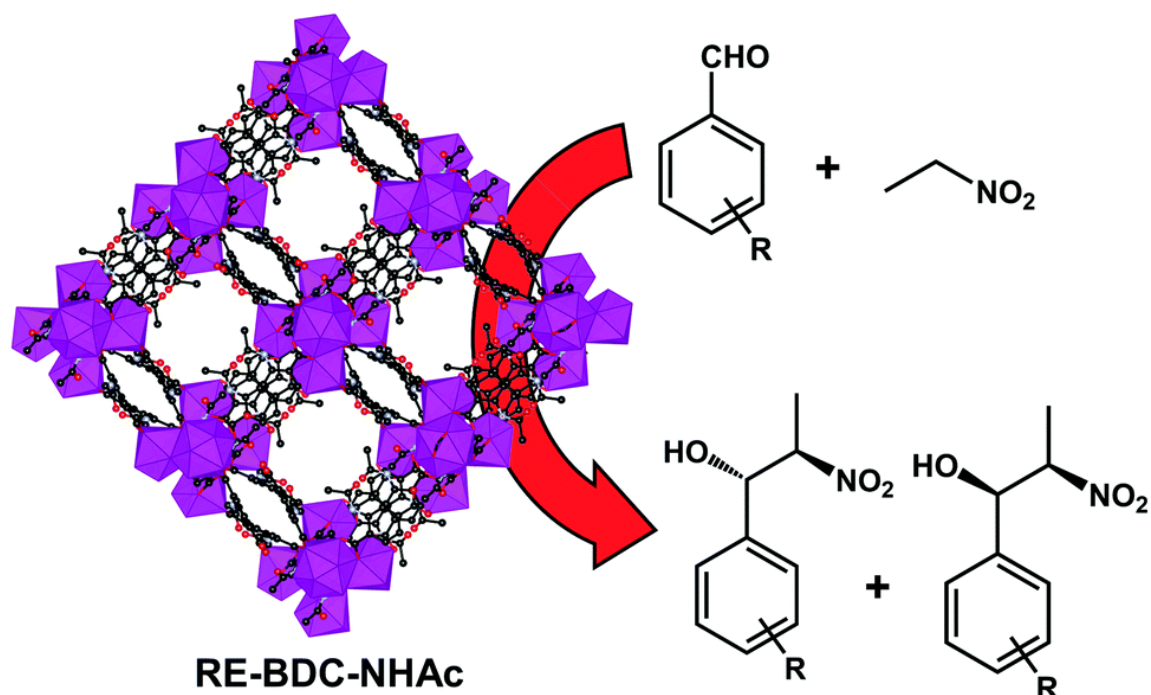
Figure 1.14. Henry (nitroaldol) reaction catalysed by RE-BDC-NHAc. La, Ce, Sm = purple, C = black, O = red, N = light blue. Hydrogen atoms omitted for clarity.

1.7. Scope of Thesis

Despite H_2BDC being an inexpensive linker that could, in essence, be used to synthesise RE(III)-UiO-66 analogues, to this date there is no example of this in literature. The following two chapters will explore the design, synthesis, and optimisation of the family of RE(III)-UiO-66 and discuss their characterisation and properties for the future goal of using these materials as catalysts.

Chapter 2 describes the design, synthesis, optimisation, and initial characterisation of a series of RE(III)-UiO-66 analogues (RE = Y(III), Eu(III), Gd(III), Tb(III), Ho(III), Er(III), Tm(III), and Yb(III)) which precipitate as crystalline powders under the tested conditions. It was determined that these materials are isoreticular to Zr-UiO-66, and that they could be potential catalysts if their stability can be optimised.

Chapter 3 discusses the synthesis of single crystals of the series of RE(III)-UiO-66 analogues and their subsequent characterisation by SCXRD. Some insights regarding the structures of RE(III)-UiO-66 analogues are drawn from the observed trends in bond lengths across the series and potential explanations for the observed behaviour are given.

Chapter 2

Synthetic Approaches for Accessing Rare-Earth Analogues of UiO-66

2.1. Introduction

Metal–organic frameworks (MOFs) are a family of structurally diverse and porous materials constructed via the concatenation of metal ions, or clusters, with organic ligands, known as linkers, extending in 2- or 3-dimensions.[19,20] These inorganic and organic building units act as nodes and vertices in a topological net, ciphered according to Reticular Chemistry Structure Resource (RCSR) by a three-letter code, such as **bct**, **fcu** or **spn**, representing the uniqueness of that net's connectivity.[48] Through the use of reticular chemistry as a design strategy, MOFs with specific properties and architectures (or nets), can be built by carefully selecting the inorganic and organic building units, also known as secondary building units (SBUs), that will constitute it.[45,46] The properties of the MOF, dictated in part by the choice of SBUs, will thus determine its potential in applications, within which catalysis,[11,31] gas adsorption,[27,29] chemical sensing,[34] water treatment,[35,37] and many more can be found.[7,154,155]

Among the various MOF families, Zr-based MOFs have been extensively studied due to their high stability, Lewis acidity, and structural tunability, making them attractive for diverse applications. In particular, there is a substantial amount of interest in Zr-MOFs containing the hexanuclear metal-oxide cluster, $[Zr_6O_4(OH)_4]^{12+}$, as an SBU[51,93,156] with the most well-known and well-studied example being Zr-UiO-66.[50] Zr-UiO-66 is comprised of 12-connected (12-c) Zr-hexanuclear clusters bridged together by 1,4-benzenedicarboxylate (H_2BDC), a 2-c linker, giving rise to a 12,2-c (also known as just 12-c) **fcu** net.[52] To this day, Zr-UiO-66 and its diverse analogues and derivatives have been studied for several different applications.[50] Focusing on the inorganic component alone, several tetravalent ions have been used in the syntheses of isostructural BDC-containing analogues M-UiO-66 (M = Hf(IV), Ce(IV), Th(IV), U(IV), Pu(IV) and Np(IV)).[50]

Another intriguing family of MOFs with diverse structures and properties are those comprised of rare-earth (RE) elements. RE elements include the 15 lanthanoids from the *f*-block plus Y and Sc. The RE metals located in the *f*-block possess unique electronic properties dictated by their 4*f* electron configuration, allowing RE-MOFs to be explored for magnetic and optoelectronic applications, in addition to the traditionally studied applications of MOFs.[44] Using

RE(III) ions to form inorganic SBUs, a vast library of MOFs has been developed, many with unique structures and topologies that result from the variability in the coordination environment of RE(III) ions.[17,40,42]

Much like other MOFs, RE-MOFs with different types of inorganic SBUs have been reported, including single ion-,[157,158] chain-,[159,160] or cluster-based SBUs.[15] Similar to tetravalent ions, RE(III) ions can be used to construct hexanuclear clusters that are structurally similar to that of Zr-UiO-66. Eddaoudi *et al.* demonstrated that the synthesis of these hexanuclear RE-clusters is possible by using alpha-fluorinated acids as modulators.[15] As such, these clusters have been used to synthesise a handful of RE-MOFs, some of them isostructural to Zr-UiO-66 with functionalised linkers.[72,73] However, to this date, RE-UiO-66 analogues, with non-functionalised BDC linkers, have not been reported in literature. Herein, we present the synthesis and characterisation of a series of isostructural RE-UiO-66 analogues prepared from the commercially available, and cost-effective BDC linker (**Figure 2.1**). The resulting new family of RE-MOFs, RE-UiO-66 (RE = Y(III), Eu(III), Gd(III), Tb(III), Ho(III), Er(III), Tm(III), Yb(III)), exhibits both high surface area and good thermal stability. Furthermore, we provide alternatives to troubleshoot the synthesis since its reproducibility can be challenging due to solvent quality. This synthesis of RE-analogues of UiO-66 will allow for the addition of RE-UiO-66 to the MOF repertoire.
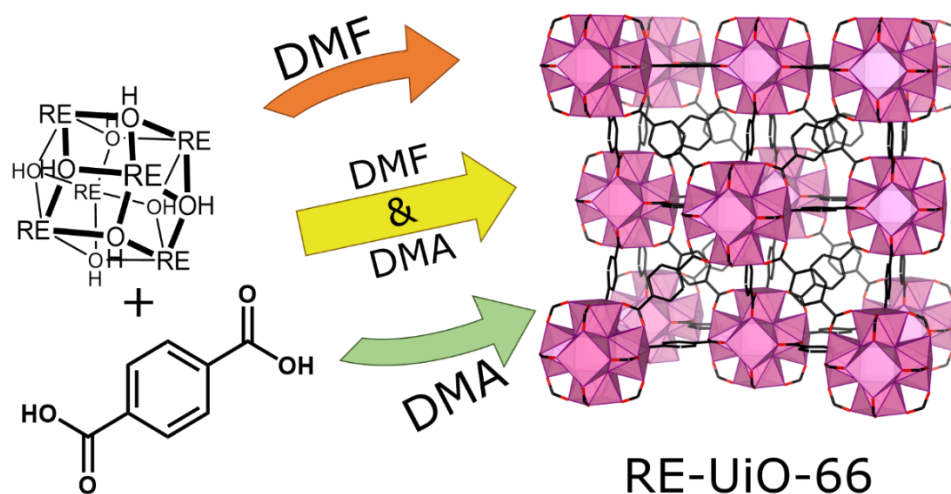
Figure 2.1. Schematic representation of the assembly of RE-UiO-66. The arrows represent the multiple solvent combinations used. Colour scheme: RE = pink, O = red, C = black. Hydrogens omitted for clarity.

2.2. Experimental Procedures

2.2.1. General Materials and Methods

All solvents and reagents were purchased from commercial sources. N,N-dimethylformamide (DMF), N,N'-dimethylacetamide (DMA), acetone, and nitric acid (70%) were purchased from Fisher Scientific (Fisher Chemical). $Y(NO_3)_3 \cdot 6H_2O$, $Eu(NO_3)_3 \cdot 6H_2O$, $Gd(NO_3)_3 \cdot xH_2O$, $Tb(NO_3)_3 \cdot xH_2O$, $Ho(NO_3)_3 \cdot xH_2O$, $Er(NO_3)_3 \cdot xH_2O$, $Tm(NO_3)_3 \cdot xH_2O$, and $Yb(NO_3)_3 \cdot xH_2O$ were purchased from Alfa Aesar. 2,6-difluorobenzoic acid (2,6-DFBA) was purchased from Combi-Blocks. H_2BDC was purchased from Acros Organics. NMR solvents D_2SO_4 and DMSO-d_6 were purchased from Alfa Aesar. All solvents and chemicals were used without further treatment.

Single crystal X-ray diffraction (SCXRD) data for Tm-UiO-66 was measured on a Bruker D8 Venture diffractometer equipped with a Photon 200 area detector, and *IμS* microfocus X-ray source (Bruker AXS, Cu*K*α source). Measurements were carried out at 253 K. The crystal diffracted weakly at high angles. Structure solution was carried out using the SHELXTL package from Bruker.[161] The parameters were refined for all data by full-matrix-least-squares or F2 using SHELXL.[162] It should be noted that disordered molecules (water, DMA, and dimethylammonium) in the MOF pores, which could not be reliably modelled using discrete atoms, were subtracted by SQUEEZE, using the PLATON software.[109] All of the nonhydrogen atoms were refined with anisotropic thermal parameters. Hydrogen atoms were placed in calculated positions and allowed to ride on the carrier atoms. All hydrogen atom thermal parameters were constrained to ride on the carrier atom. See **Table A.1** in the appendix.

Powder X-ray diffraction (PXRD) patterns were collected on a Bruker D2 Phaser diffractometer (measurements made over a range of $4° < 2\theta < 20°$ in 0.02° step with a 0.200 s scanning speed) equipped with a LYNXEYE linear position sensitive detector (Bruker AXS, Madison, WI). Neat samples were smeared directly onto the silicon wafer of a proprietary low-zero background sample holder. Data was collected using a continuous coupled $\theta/2\theta$ scan with Cu*K*α ($\lambda = 1.54178$ Å). No important reflections can be observed after 20° 2θ for all the samples.

Variable temperature (VT) PXRD patterns were collected on a Bruker D8 Advance diffractometer (measurement made over a range of $2° < 2\theta < 40°$ in 0.02° step with a 0.200 s scanning speed) equipped with a LYNXEYE linear position sensitive detector (Bruker AXS, Madison, WI). Neat samples were smeared directly onto the silicon wafer of a proprietary low-

zero background sample holder. Data was collected using a continuous coupled $\theta/2\theta$ scan with Ni-filtered Cu$K\alpha$ (λ = 1.54178 Å). The setup was equipped with an Anton Paar CHC$^+$ chamber. Diffractograms were collected in a stepwise fashion, and after each collection (*ca.* 7 min), the temperature in the chamber was raised in intervals of 5 °C at a rate of 1 °C min^{-1} and a new collection started.

^{1}H-NMR spectra were recorded on a 300 MHz Bruker spectrometer and the chemical shifts were referenced to the residual solvent peaks. ~5 mg of activated sample was digested in D_2SO_4 and diluted with DMSO-d_6. The digestion was carried on in a vial wherein the sample was attacked first with around 10 drops of D_2SO_4 and sonicated for 10 min. The slurry was then diluted with DMSO-d_6 and loaded into an NMR tube. This experiment was done only to confirm the presence of BDC^{2-} in the structure of the synthesised material. For identifying the cation, ~5 mg of activated sample was digested in a NaOH solution in D_2O (40% m/m) with sonication for 30 min. The final volume was brought up to 0.8 mL. The mixture was then centrifuged, and the supernatant was loaded into an NMR tube.

Inductively coupled plasma – mass spectrometry (ICP-MS) data was measured on an Agilent 7500 Series. ~ 1 mg of the activated RE-UiO-66 (RE = Y(III), Tb(III), Er(III), Tm(III), Yb(III)) was weighed and digested in 750 µL H_2SO_4 at high temperatures in a sand bath for 24 h. This solution is diluted with deionised H_2O to a final volume of 10 mL. Finally, an aliquot of this solution is diluted by 50 times and injected in the equipment. Calculations were done assuming the following formula for the activated sample: $[(CH_3)_2NH_2]_2[RE_6(OH)_8(BDC)_6]$. A higher experimental percentage of metal in the material than theoretical percentage is indicative of the presence of linker defects in the structure.

Diffuse reflectance infrared spectra were recorded using a Thermo Scientific Nicolet 6700 FT-IR equipped with a MCT detector with a resolution of 1 cm^{-1} in the range of 4000-450 cm^{-1}. Diffuse reflectance infrared Fourier transformed spectroscopy (DRIFTS) was used to confirm the presence of the carboxylate group from the linker. The samples were run after activation with no further treatment.

Thermogravimetric analysis (TGA) was carried out in a TGA/DSC 1 from Mettler Toledo, from room temperature to 800 °C at a rate of 5 °C/min under air. For TGA analysis, ~ 5 mg of the activated RE-UiO-66 (RE = Y(III), Eu(III), Tb(III), Er(III), Tm(III), Yb(III)) was weighed with no further treatment. The final percentage of the RE$_2$O$_3$ residue is adjusted for the presence of

humidity below 100 °C and then compared to the expected value for the perfect formula, [(CH3)2NH2]2[RE6(OH)8(BDC)6]. **Figure 2.2** shows the procedure use to estimate the experimental percentage. A higher experimental percentage RE_2O_3 than the expected value is indicative of the presence of missing linkers.
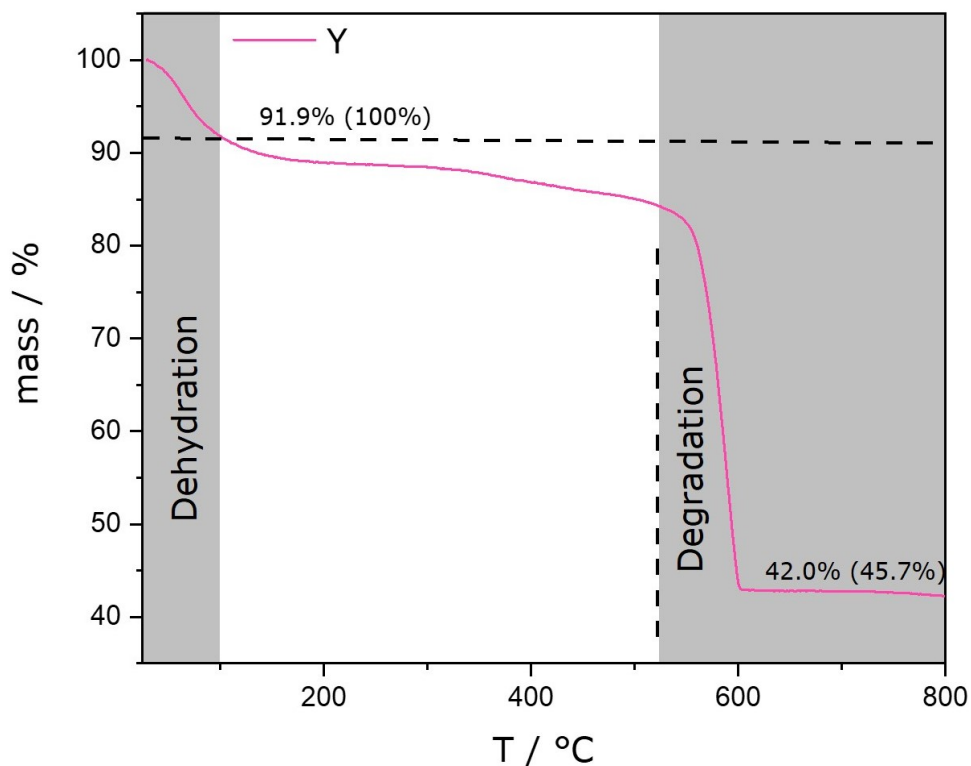
Figure 2.2. TGA plot for Y-UiO-66 detailing how the experimental Y_2O_3 percentage is estimated.

Scanning electron microscopy (SEM) images were collected on a Phenom ProX desktop SEM.

MOF samples were activated using a Micromeritics SmartVacPrep instrument equipped with a hybrid turbo vacuum pump. Nitrogen adsorption/desorption isotherms were measured at 77K on a Micromeritics TriStar II Plus instrument.

2.2.2. Synthesis

RE-UiO-66 in DMF (RE = Y(III), Ho(III), Er(III), Tm(III), Yb(III)): Y-, Ho-, Er-, Tm- and Yb-UiO-66 were synthesised solvothermally in 6-dram vials containing the corresponding

RE(NO₃)₃·xH₂O (0.174 mmol, assuming hexahydrate for all of them), H₂BDC (28.5 mg, 0.171 mmol), and 2,6-DFBA (440 mg, 2.78 mmol), suspended in DMF (8 mL). The vials were sealed and placed into a preheated oven at 120 °C for 36 h. The precipitates were separated via centrifugation, washed three times with fresh DMF over the course of 24 h, and later three times with fresh acetone over the course of 24 h. The material was then air-dried and activated under vacuum at 80 °C, except for Ho-UiO-66.

RE-UiO-66 in DMF:DMA (RE = Eu(III), Gd(III), Tb(III)): Eu-, Gd-, Tb-UiO-66 were synthesised solvothermally in 6-dram vials containing the corresponding RE(NO₃)₃·xH₂O (0.174 mmol, assuming hexahydrate for all), H₂BDC (28.5 mg, 0.171 mmol), and 2,6-DFBA (440 mg, 2.78 mmol), suspended in 8 mL of a DMA:DMF mixture with ratios of 7:1(Eu), 3:5(Gd) and 1:7(Tb). The vials were sealed and placed into a preheated oven at 120 °C for 48 h. The precipitates were separated via centrifugation, washed three times with fresh DMF over the course of 24 h, and later three times with fresh acetone over the course of 24 h. The material was then air-dried and activated under vacuum at 80 °C, except for Gd-UiO-66.

RE-UiO-66 in DMF with HNO₃ (RE = Y(III), Ho(III), Er(III), Tm(III), Yb(III)): Y-, Ho-, Er-, Tm- and Yb-UiO-66 were synthesised solvothermally in 6-dram vials containing the corresponding RE(NO₃)₃·xH₂O (0.174 mmol, assuming hexahydrate for all of them), H₂BDC (28.5 mg, 0.171 mmol), 2,6-DFBA (440 mg, 2.78 mmol), concentrated HNO₃ (50 µL) suspended in DMF (8 mL). The vials were sealed and placed into a preheated oven at 120 °C for 36 h. The precipitates were separated via centrifugation, washed three times with fresh DMF over the course of 24 h, and later three times with fresh acetone over the course of 24 h. The material was then air-dried.

RE-UiO-66 in DMA (RE = Y(III), Eu(III), Gd(III), Tb(III), Ho(III), Er(III), Tm(III), Yb(III)): the RE-UiO-66 were synthesised solvothermally in 6-dram vials containing the corresponding RE(NO₃)₃·xH₂O (0.174 mmol, assuming hexahydrate for all), H₂BDC (28.5 mg, 0.171 mmol), and 2,6-DFBA (440 mg, 2.78 mmol), suspended in DMA (8 mL). The vials were sealed and placed into a preheated oven at 120 °C for 72 h. The precipitates were separated via centrifugation, washed three times with fresh DMF over the course of 24 h, and later three times with fresh acetone over the course of 24 h. The material was then air-dried.

Tm-UiO-66 single crystals: single crystals of Tm-UiO-66 were synthesised solvothermally in 6-dram vials containing Tm(NO₃)₃·xH₂O (0.087 mmol, assuming hexahydrate), H₂BDC (14.3

mg, 0.085 mmol), 2,6-DFBA (220 mg, 1.39 mmol), HCl 35.5% (300 μL), in DMA (8 mL). The vials were sealed and placed into a preheated oven at 120 °C for 72 h. Octahedral crystals of approx. 80 μm crystals suitable for SCXRD were collected from the walls of the vial.

Some optimal ratios that can be used for a DMF:DMA mixture for the synthesis of RE-UiO-66 (RE = Y(III), Ho(III), Er(III), Tm(III) and Yb(III)) are 6:2 and 4:4, in case DMF alone does not give the expected product.

Zr-UiO-66 for reference was synthesised according to previously reported procedures.[52]

2.2.3. Zr_6 and RE_6 Secondary Building Unit

The metal node in Zr-UiO-66 can be defined as: $Zr_6(\mu_3\text{-OH})_4(\mu_3\text{-O})_4(\text{COO-})_{12}$ (**Figure 2.3a**), giving a net neutral charge: $(+4)*6 + (-1)*4 + (-2)*4 + (-1)*12 = 0$
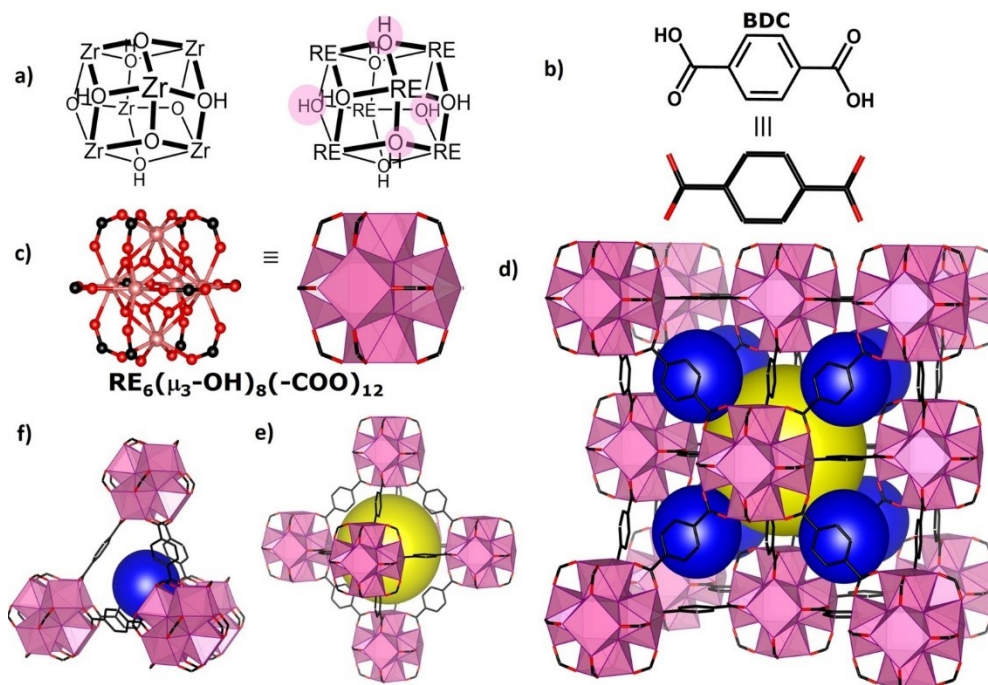
Figure 2.3. Structure of RE-UiO-66. (a) Differences between Zr- and RE-hexanuclear cluster highlighted in pink. (b) Linear 1,4-benzenedicarboxylate (BDC) linkers will connect the (c) 12-c SBU to establish (d) RE-UiO-66 with **fcu** topology. Two kinds of cages exist in the net, (e) the octahedral cage (yellow sphere), and (f) the tetrahedral cages (blue spheres).

As a result, there is no need for any charge compensating ions in Zr-UiO-66, or similar structures containing metals with oxidation state IV. The same is not true for RE(III)-based hexanuclear clusters, wherein the building block can be defined as $RE_6(\mu_3\text{-}OH)_{8\text{-}x}(\mu_3\text{-}O)_x(COO\text{-})_{12}$, for a 12-connected structure such as RE-UiO-66 (or other 12-connected structures reported in the literature). In this case, x is assigned so as to minimise the charge in the framework as much as possible. The charge is brought to its minimum within the framework when x = 0, so the charge can be calculated as follows: (+3)*6 + (-1)*8 + (-2)*0 + (-2)*6 = -2.

Bridging –OH groups are confirmed using DRIFTS (**Figure 2.4**) and the presence of DMA cations to balance the charge is confirmed by NMR (**Figure 2.5**) on an acetone exchanged and activated sample. Previous reports of similar structures define the cluster in the same way.[72,163,164]
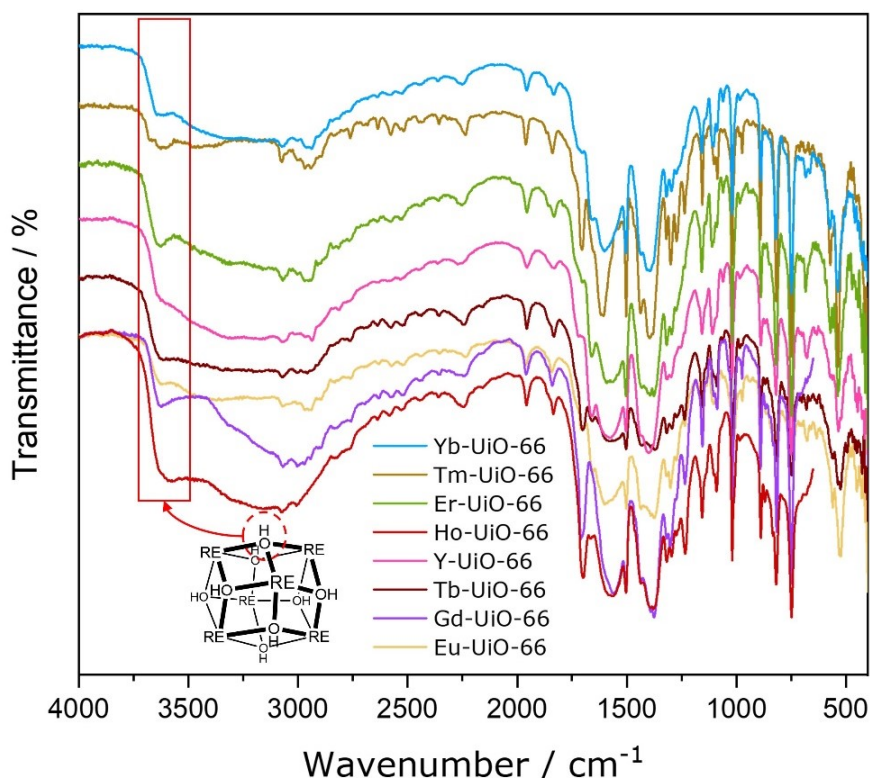
Figure 2.4. DRIFTS spectra for RE-UiO-66 (RE = Yb(III), Tm(III), Er(III), Ho(III), Y(III), Tb(III), Gd(III) Eu(III)). All materials show similar peaks, confirming that they are all isostructural. O-H stretch band from cluster is highlighted. Spectra are stacked for clarity.
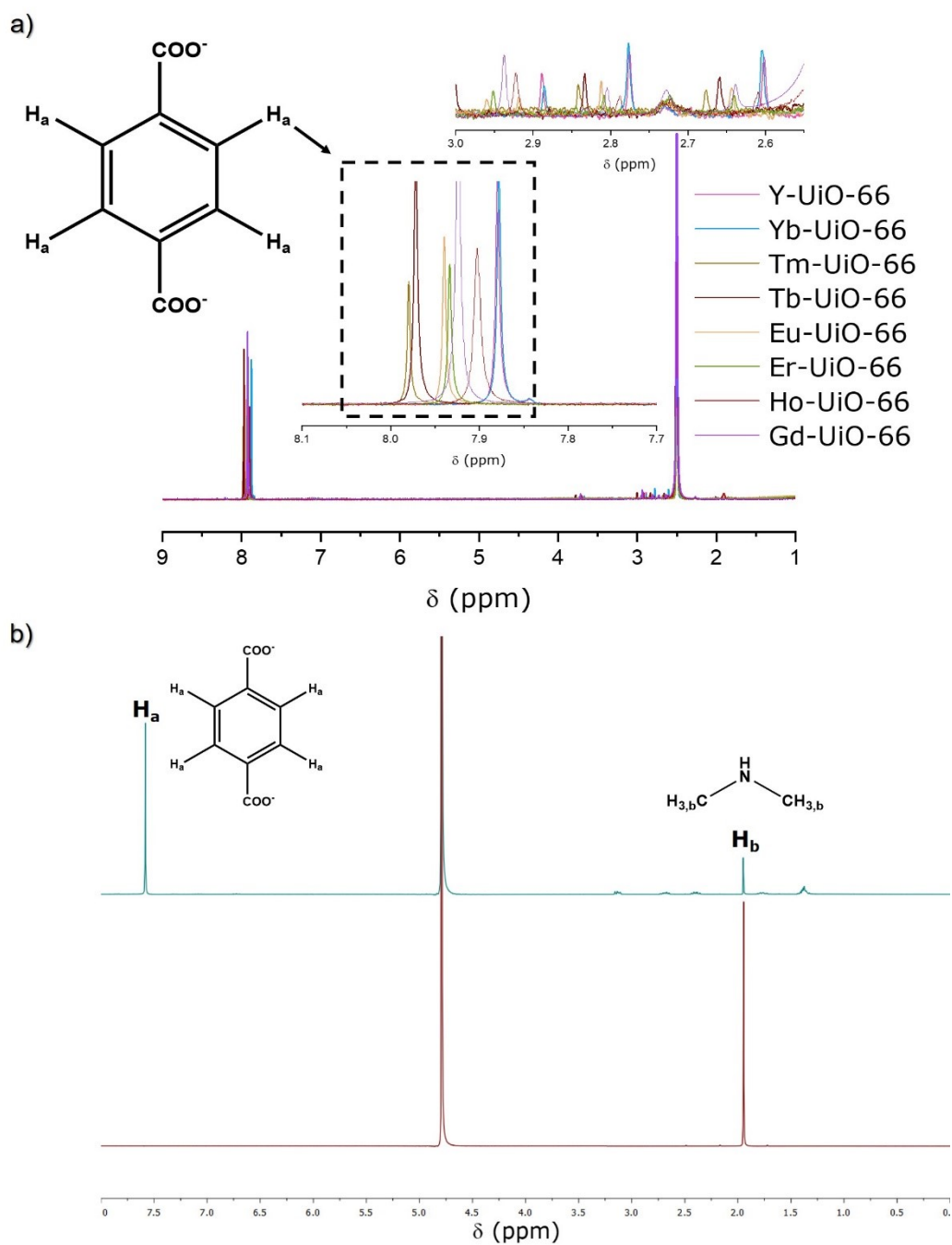
Figure 2.5. ^{1}H-NMR spectrum for (a) RE-UiO-66 (RE = Y(III), Yb(III), Tm(III), Tb(III), Eu(III), Er(III), Ho(III), Gd(III)) digested in D_2SO_4 and solubilised in DMSO-d_6, differences in chemical shift might be due to varying amounts of deuterated sulfuric acid changing solvent polarity; (b) Y-UiO-66 (top) and $(CH_3)_2NH \cdot HCl$ (bottom) digested in a mixture of D_2O and NaOH.

2.3. Results and Discussion

Solvothermal reactions between $RE(NO_3)_3 \cdot xH_2O$ (RE = Y, Eu, Gd, Tb, Ho, Er, Tm, Yb) and BDC in different N,N-dimethylformamide (DMF)/N,N-dimethylacetamide (DMA) solvent mixtures in the presence of 2,6-DFBA yield transparent, homogeneous, and polyhedral crystals corresponding to RE-UiO-66 (RE = Y(III), Eu(III), Gd(III), Tb(III), Ho(III), Er(III), Tm(III), Yb(III)) (**Figure 2.6a and 2.6b**). Initially, synthetic conditions for the precipitation of RE-UiO-66 were screened for Y-UiO-66, after which the conditions were adapted to obtain the rest of the series. Of these, Tm-UiO-66 synthesised in DMA in the presence of HCl, produced crystals large enough (*ca.* 80 μm) for SCXRD, which indicated the following formula: $[(CH_3)_2NH_2]_2[Tm_6(\mu_3-OH)_8(BDC)_6] \cdot (DMA)_6 \cdot (H_2O)_3$ (see SI for detail). Unlike M(IV) analogues of UiO-66, RE(III)-UiO-66 is anionic in nature, $[RE_6(\mu_3-OH)_8(BDC)_6]^{2-}$, and the charge must be compensated with counterions to achieve charge neutrality. Both in DMF and in DMA solutions, $[(CH_3)_2NH_2]^+$ can be found as a product of decomposition at high temperatures, providing the cation necessary for balancing the anionic MOF.[15] The phase purity of the RE-UiO-66 series was confirmed by comparison to the calculated PXRD obtained from the single crystal data of Tm-UiO-66, and all materials are confirmed to be isostructural to Zr-UiO-66 (**Figure 2.6c**). The lattice parameter for Zr-UiO-66 is 20.7 Å, whereas it is 21.2 Å for Tm-UiO-66, an expected increase based on the differences in ionic radius for Zr(IV) (0.84 Å, coordination number: 8) and Tm(III) (0.99 Å, coordination number: 8). A topological analysis of Tm-UiO-66 corroborated its topology as **fcu** assembled from 12-c $[Tm_6(\mu_3-OH)_8(O_2C-)_{12}]^{2-}$ SBUs, wherein the carbon in the carboxylic acid acts as a point of extension. Analogous to M(IV)-UiO-66, RE-UiO-66 contains two types of cages: an octahedral cage located at the centre of the unit cell and face-sharing with 8 tetrahedral cages (**Figure 2.3e and 2.3f**). The diameters of these cages are found to be *ca.* 12 Å and *ca.* 7 Å, respectively, accessible through triangular windows with apertures of *ca.* 6 Å.
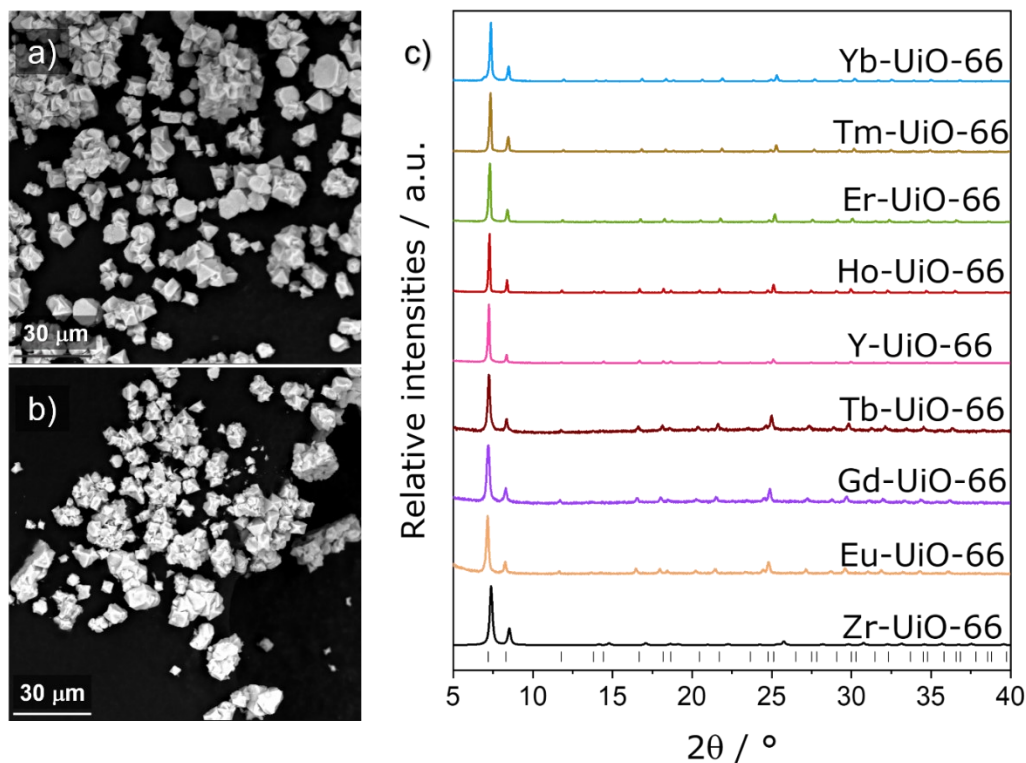
Figure 2.6. SEM image showing the polyhedral crystals for (a) Tm-UiO-66 and (b) Y-UiO-66; (c) Stacked PXRD patterns for all RE-UiO-66 analogues, and Zr-UiO-66 for comparison. Vertical lines are the allowed reflections from the Tm-UiO-66 crystal structure.

After several synthetic attempts, optimised conditions were found to synthesise RE-UiO-66 (RE = Y(III), Ho(III), Er(III), Tm(III), Yb(III)) using DMF as the reaction solvent. This procedure, however, could not be translated to Eu(III), Gd(III), or Tb(III), which gave low quality, impure and/or completely different materials. DMF is the most widely used solvent for MOF synthesis, owing in part to its high boiling point, polar aprotic nature, and hydrolytic decomposition to give dimethylamine (a base that can aid with deprotonation of carboxylic acid linkers) and formate (a ligand that can cap and stabilise inorganic SBUs).[165] DMA is a solvent with similar properties, albeit with a slower rate of decomposition to yield dimethylamine and acetate at high temperatures under acidic conditions.[166] As such, we explored the use of DMA for the synthesis of RE-UiO-66, in an attempt to modify the linker deprotonation process. Interestingly, the Eu(III) and Tb(III) analogues, as well as the others previously obtained in DMF, were obtained using only DMA as the solvent. Given that DMA is significantly more expensive than DMF,[166] we sought to optimise the procedure using the minimum necessary amount of DMA. It should be

32

noted that in order to precipitate materials of appreciable quality, different mixtures of DMF/DMA are required. Specifically, a ratio of 7:1 (DMA:DMF) is needed for Eu-UiO-66, 3:5 for Gd-UiO-66, while 1:7 is enough for Tb-UiO-66. Coincidentally, the three RE-UiO-66 analogues that require the presence of this auxiliary solvent to form, Eu(III), Gd(III), and Tb(III), are the ones with the largest ionic radii in the series. This suggests that a more sterically bulky solvent with a slower decomposition rate may be required when RE-UiO-66 comprised of ions with larger ionic radii is desired. Nonetheless, attempts to synthesise RE-UiO-66 with lighter lanthanoids (La(III), Ce(III), Pr(III), and Nd(III)) using this methodology have so far been unsuccessful.

On the other hand, the formation of RE-UiO-66 (RE = Y(III), Ho(III), Er(III), Tm(III), and Yb(III)) in DMF was found to be susceptible to variability between batches of DMF, where batches coming from different, or even the same, commercial sources give different results (**Figure 2.7a**). This reproducibility issue can be solved by replacing some of the DMF in the reaction mixture with DMA, but since the objective was to keep the amount of DMA to a minimum, a screening of different monoprotic acids (HCl and HNO_3) was performed. It was found that a molar ratio of 160:1 of DMF to HNO_3 was sufficient to allow for the formation of RE-UiO-66, without the addition of DMA, in instances where DMF alone resulted in impure samples. Owing to our observations, which include results from testing over 100 reaction conditions, we have outlined a series of steps to troubleshoot the reaction conditions if RE-UiO-66 is the desired product:

1. Follow the reaction as it is described in the synthesis section, using DMF as the solvent
2. If the product shows impurities (**Figure 2.7a**), add HNO_3 in a 160:1 ratio (DMF:HNO_3) (for RE = Y(III), Ho(III), Er(III), Tm(III), Yb(III)) (**Figure 2.7b**)
3. If the addition of HNO_3 cannot be adjusted to form a pure material, replace DMF with DMA (**Figure 2.7c**), either partially or completely (for RE = Y(III), Eu(III), Gd(III), Tb(III), Ho(III), Er(III), Tm(III), Yb(III). This synthetic procedure is highly robust and reproducible.
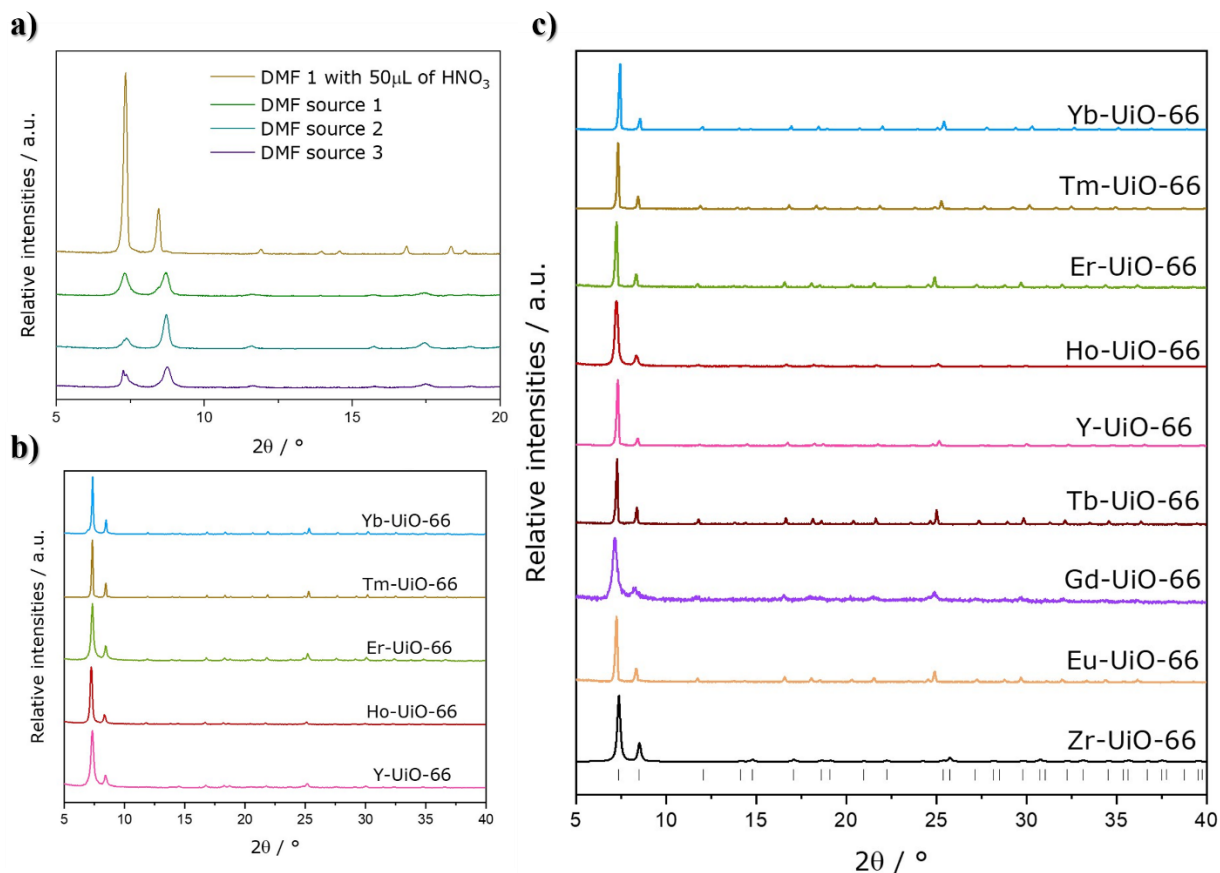
Figure 2.7. Stacked PXRD diffractograms of (a) the product of the synthesis in DMF for the as-synthesised Tm-UiO-66 using different batches and HNO$_3$; (b) the product of the synthesis in DMF with HNO$_3$ for as-synthesised RE-UiO-66 (RE = Y(III), Ho(III), Er(III), Tm(III), Yb(III)); and (c) product of the synthesis in DMA for RE-UiO-66 (RE = Eu(III), Gd(III), Tb(III), Y(III), Ho(III), Er(III), Tm(III), Yb(III)). Zr-UiO-66 can be found at the bottom for comparison.

Previous reports have shown the utility of 2-fluorobenzoic acid (2-FBA) as a modulator for the generation of the hexanuclear RE-cluster SBU, as well as other lower and higher nuclearity RE-clusters.[69] Although 2-FBA has been used to synthesise some RE-UiO-66 isostructures in DMF,[15,44] in our hands, and using H$_2$BDC as a linker, it did not yield the target RE-UiO-66 in a solution containing DMF. Other fluorinated modulators, including trifluoroacetic acid and fluoro-substituted benzoic acid derivatives were thus explored under various conditions. Only 2,6-DFBA was found to be a successful modulator for obtaining the desired material when using DMF as the solvent. It was found nonetheless that 2-FBA in combination with DMA can yield Y-UiO-66 (**Figure 2.8**).
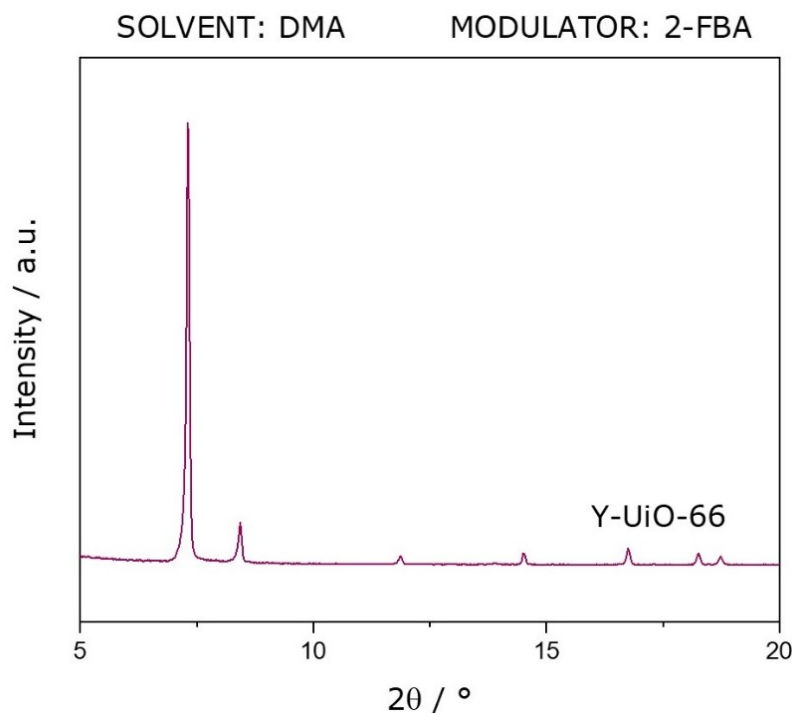
Figure 2.8. PXRD of Y-UiO-66 synthesised in DMA with 2-FBA as the modulator.

To confirm the surface area and porosity of the RE-UiO-66 series, various activation procedures were attempted, and N_2 adsorption/desorption analysis was performed. After exposure of Y-UiO-66 to several activation conditions (**Table 2.1**), it was found that an activation temperature of 80 °C for a time lapse of 20 h under vacuum was sufficient to activate the material and obtain a BET surface area comparable to that reported for Zr-UiO-66 (*ca.* 1200 m²/g).[167] N_2 adsorption/desorption measurements of RE-UiO-66 analogues activated at 80 °C (**Figure 2.9**) show Type-I isotherms, expected for UiO-66 isostructural materials, with apparent Brunauer-Emmett-Teller (BET) surface areas (SAs) and pore volumes of 1360 m²/g and 0.56 cm³/g (Y), 1160 m²/g and 0.48 cm³/g (Eu), 1070 m²/g and 0.43 cm³/g (Gd), 1030 m²/g and 0.43 cm³/g (Tb), 1000 m²/g and 0.41 cm³/g (Ho), 1190 m²/g and 0.49 cm³/g (Er), 1010 m²/g and 0.42 cm³/g (Tm), and 1080 m²/g and 0.43 cm³/g (Yb). Differences in BET SA between RE-UiO-66 analogues can be attributed to the variable atomic mass of the RE-elements, and due to the fact that activation procedures were only optimised for Y-UiO-66 and then applied to the rest of the RE-UiO-66 series. In addition, pore size distribution analysis by non-local density functional theory (NLDFT) reveals that the octahedral pores have diameters of *ca.* 10 Å for the entire series.

35

Table 2.1. Activation conditions attempted for Y-UiO-66.

Temperature (°C)	Time (h)	Surface area (m²/g)
150	24	1060
130	24	1350
120	24	1350
80	20	1370
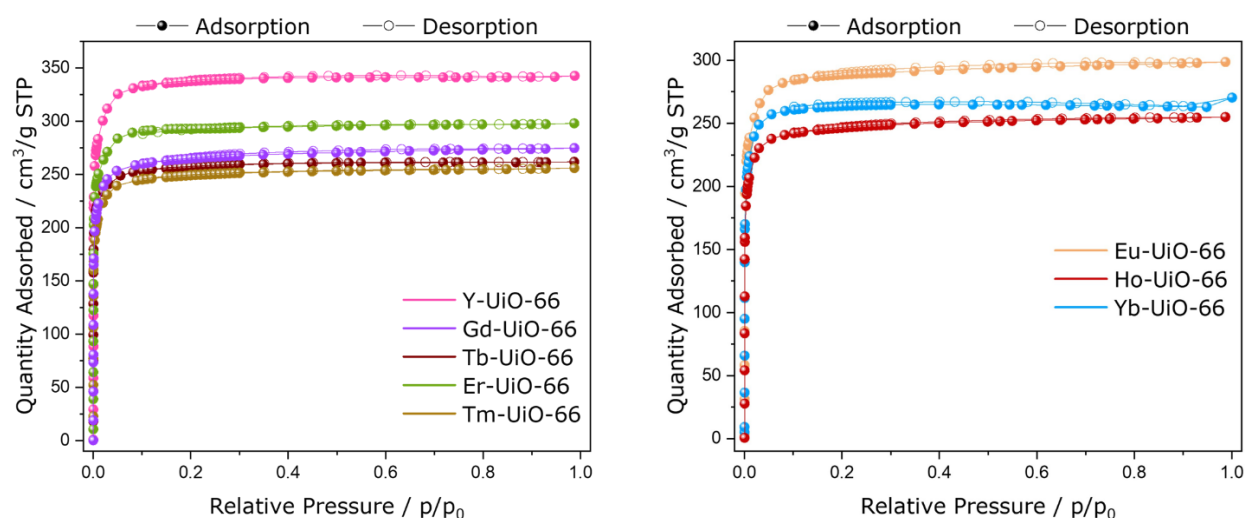
Figure 2.9. Nitrogen adsorption-desorption isotherms for all the synthesised analogues of RE-UiO-66.

To our surprise, upon revaluation of the N_2 isotherm for Y-UiO-66, 2 to 3 days after the initial measurement, the isotherm was changed, and the BET SA was reduced significantly, eventually reaching a value of 0 m²/g after 7 days. Given that such a reduction in SA is likely to be accompanied by a loss of crystallinity, PXRD measurements were collected 2 to 7 days post activation for all materials, showing a loss in crystallinity, corresponding to a decrease in reflection intensity of 60-90 % after two days (**Figure 2.10a**). Similarly, when the solvent exchanged Y-UiO-66 was left under ambient conditions in a capped vial for more than 40 days a reduction can be observed as well (**Figure 2.10b**). Contrary to what is observed for Zr-UiO-66, thermal activation of RE-UiO-66 under vacuum appears to lead to its degradation or collapse a short time after the process. We hypothesise that removal of $(CH_3)_2NH_2^+$ during activation might be

36

occurring, and thus, it is affecting the stability of the framework. Further research is being done in this respect.
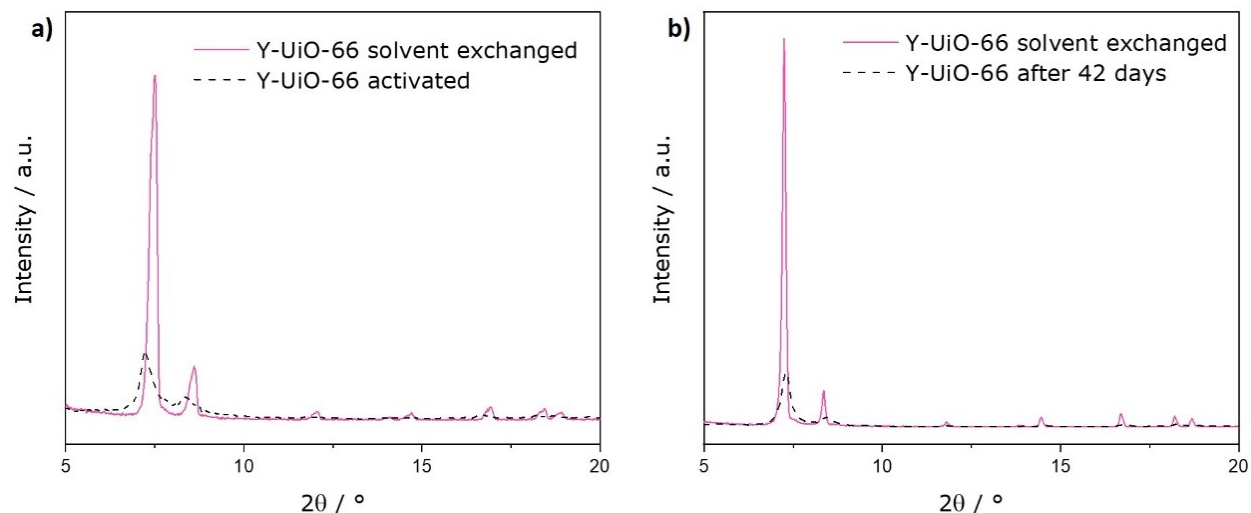
Figure 2.10. PXRD patterns showing loss of crystallinity of Y-UiO-66 (a) after activation, and (b) when sitting in the vial air-exposed for 42 days.

The thermal stability of RE-UiO-66 (RE = Y(III), Eu(III), Tb(III), Er(III), Tm(III), Yb(III)) was investigated through TGA on activated samples (**Figure 2.11**) under air. In all cases, the thermogram shows a loss in mass due to the loss of moisture below 100 °C, followed by a major mass loss at *ca.* 500 °C. Eu-UiO-66 shows a slightly different thermogram than the rest of the RE-UiO-66 series and it decomposes at a lower temperature (*ca*. 450 °C *vs. ca*. 500 °C). This is likely due to the fact that Eu(III) is the weakest Lewis acid in the series making the Eu-O bond more labile. Analysis of the residue mass % (assumed to be RE_2O_3), as well as ICP-MS data (**Tables 2.2** and **2.3**) suggest that all RE-UiO-66 analogues contain some defects (i.e. missing linkers or missing nodes) in their structure, similar to what is observed for Zr-UiO-66.[167] Additionally, variable temperature VT-PXRD was performed on non-activated Y-UiO-66 to corroborate that no major changes in the structure are occurring upon heating (**Figure 2.12**). Indeed, Y-UiO-66 does not undergo major changes or loss of crystallinity when heated up to 200 °C. This highlights the thermal stability of the material pre-activation, being comparable to that of Zr-UiO-66.[52]
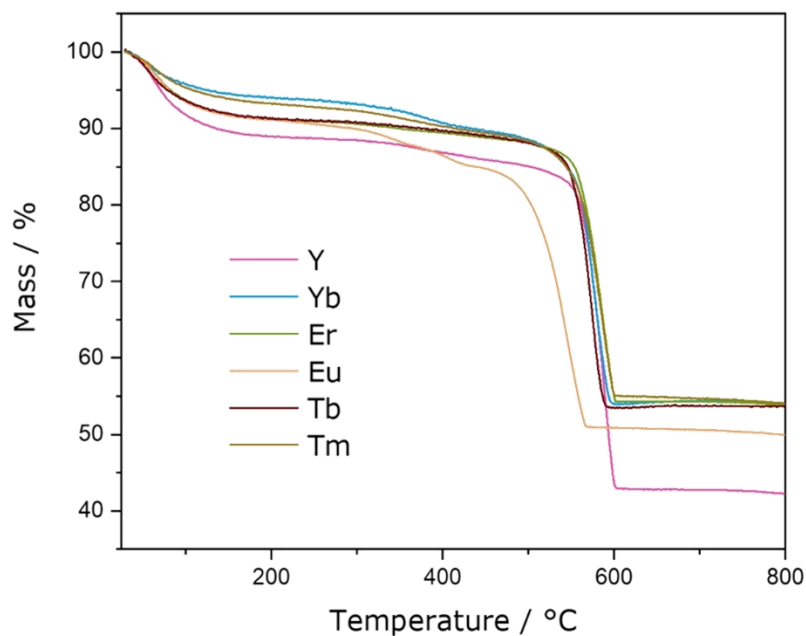
Figure 2.11. TGA plots for RE-UiO-66 (RE = Y(III), Yb(III), Er(III), Eu(III), Tb(III), Tm(III)).

Table 2.2. ICP values for the RE-UiO-66 (except Eu, Gd, and Ho).

RE	%$_{RE\ theoretical}$	%$_{RE\ ICP}$
Y	30.55	32.47
Tb	44.02	49.65
Er	44.99	48.43
Tm	45.53	50.44
Yb	46.12	46.93

Table 2.3. TGA %$_{REoxide}$ for RE-UiO-66.

RE	%$_{REoxide\ theoretcial}$	%$_{REoxide\ TGA}$
Y	38.8	45.7
Eu	49.7	55.2
Tb	50.7	57.0
Er	51.5	57.2
Tm	52.0	57.6
Yb	52.5	56.6
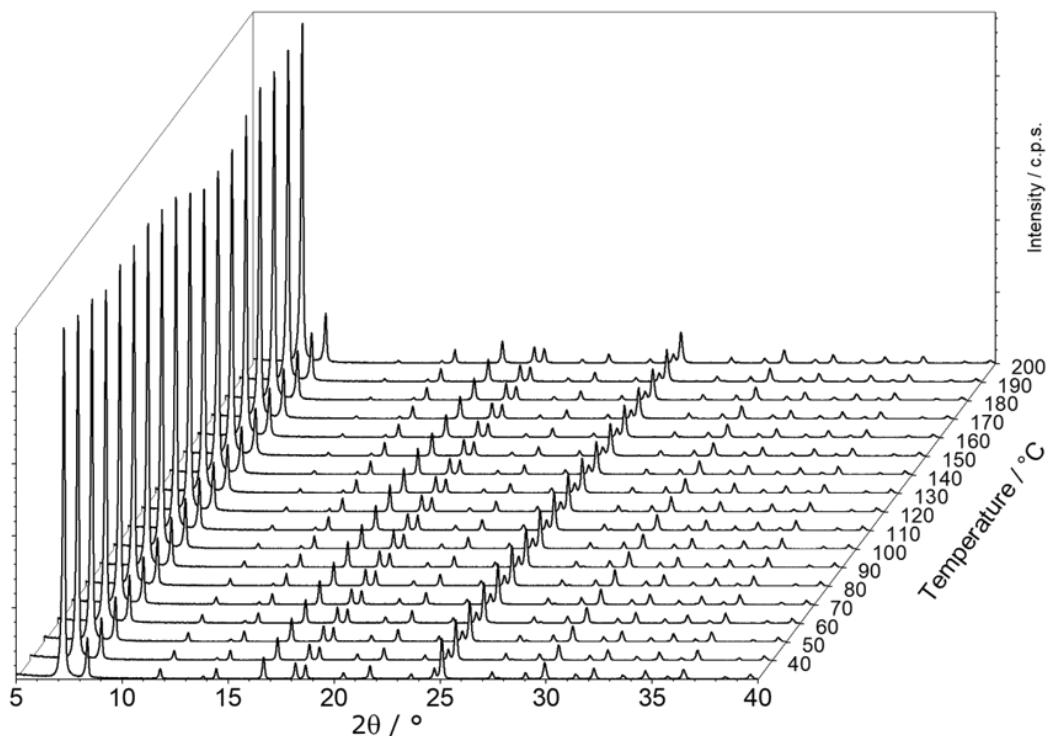
Figure 2.12. VT-PXRD of Y-UiO-66 from 25 °C to 200 °C.

2.4. Conclusions

In conclusion, we report here the synthesis and characterisation of a family of RE-UiO-66 (RE = Y(III), Eu(III), Gd(III), Tb(III), Ho(III), Er(III), Tm(III), Yb(III)). This series of RE-UiO-66 materials are analogues of the archetypical Zr-UiO-66, synthesised using BDC linker with RE-metals for the first time. We provide a series of steps that can be taken to obtain the various RE-UiO-66 analogues, in the event that solvent quality affects the reproducibility of the synthetic protocol. All RE-UiO-66 analogues demonstrate permanent porosity with a range of surface areas from 1000 to 1370 m^2/g. It was found that after activation the material tends to degrade with time and currently this phenomenon is being studied in more detail. However, pre-activation these MOFs demonstrate high thermal stability where VT-PXRD of Y-UiO-66 shows that there is no phase transition or notable decomposition occurring in the range of 25 °C – 200 °C.

Chapter 3

Probing Trends in the Stability of RE-UiO-66 Analogues through Analysis by Single Crystal X-ray Diffraction

3.1. Introduction

In the past few decades, metal–organic frameworks (MOFs) have seen an increase in research interest.[40,168] MOFs are self-assembled structures produced by the combination and concatenation of inorganic building units (i.e., ions, clusters, or chains) with multitopic organic ligands, or linkers, which act as the organic building units.[45] The smallest repeating unit, which is often a combination of the inorganic node and surrounding organic linkers is commonly termed the secondary building unit (SBU). It is due to their structural characteristics, such as high porosity and immense free volume with values up to 90%,[21–23] that several potential applications of MOFs have been explored, including but not being limited to gas adsorption,[27–29] catalysis,[11,30–32] chemical sensing,[33,34] and water treatment.[35–37]

Although there are examples of amorphous MOFs,[169] long-range order — i.e. crystallinity — is a structural feature that dominates the vast majority of MOFs reported as of today. Crystalline materials are advantageous to study due to their known composition, and constant density, as well as the uniform distribution of functionality. In MOFs, crystalline structures can be used to determine the position of adsorption sites,[101] proof of post-synthetic modification,[103,104] and precise identification of pore-occupying species.[105] Conventionally, there are two methods used to determine crystallinity in MOFs. If the synthesised MOF crystallites have a size < 50 μm then the crystalline powder can be examined using powder X-ray diffraction (PXRD).[75] Upon obtaining a diffractogram, it can be compared to a simulated pattern for a known structure to confirm phase purity and overall topology of a MOF. Alternatively, and in conjunction with other characterisation techniques, PXRD can be used to obtain structural information about a newly synthesised material through the Rietveld refinement method, which involves modelling the position of the ions in the unit cell.[51,170] When the crystallite size is > 50 μm, then the more powerful single crystal X-ray diffraction (SCXRD) technique can be used to obtain absolute structural information of the MOF.[75,102] To this day, obtaining a crystal structure for a newly synthesised MOF is considered a difficult task since there is not, in most cases, a significant difference between growth and

nucleation rates leading to the precipitation of crystalline powders rather than suitable single crystals.[171] Furthermore, solving and refining MOFs crystal structures can be very challenging due to i) the presence of pore-occupying species, which are often highly disordered and ii) high possibilities of crystal twinning due to their high symmetry.[102]

Rare earth (RE) is a denomination containing yttrium, scandium, and the *f*-block elements.[40] There has been a lot of attention focused on the synthesis of RE-MOFs because of the attractive coordination environments, and appealing chemistry of the lanthanoid elements due to their *f*-electrons.[40] RE elements behave chemically similarly — i.e., oxidation state and coordination number (CN) — and can give rise to isoreticular structures of RE-MOFs in which the only structural difference is the elemental composition of the inorganic SBU.[74,172,173] Thus, they provide the perfect platform to perform systematic studies on the effects of ionic radii on the chemical and physical stability of isoreticular MOFs.[173]

RE elements are known for their ability to produce complex structures such as multinuclear-oxo clusters, with the most well-known cases in the MOF field being the RE(III)-hexanuclear cluster (RE_6-cluster).[29,67,150] There are two variants of the RE_6-cluster which differ from each other in the presence of an interstitial μ_6-O bridging the six RE ions in the cluster together (**Figure 3.1**). One of these clusters resembles the Zr_6-cluster used in the synthesis of the archetypical MOF Zr-UiO-66, and was first theorised as a potential SBU in the formation of isoreticular **fcu** structures by Eddaoudi *et al.*[15,29] In their work, they found that a fluorinated linker, or modulator, was needed to form the cluster *in-situ* (a-RE_6-cluster). To the best of our knowledge, only a few instances of this type of cluster are used to form RE_6-cluster based MOFs with the light lanthanoids [Nd(III), and Sm(III)],[73,74,164] with no examples of clusters containing Pr(III) or lighter lanthanoids. Conversely, instances of the other type of RE_6-cluster (b-RE_6-cluster) have been found by Gándara *et al.*, for RE = La(III), Nd(III), and Pr(III); using very different reaction parameters.[149,150] It should be noted that a Ce(IV)$_6$-cluster exists and has been used as a SBU in the design and synthesis of MOFs, but in the case of Ce(III) only chain nodes have been observed.[60,174]

a-RE$_6$-cluster   **b-RE$_6$-cluster**
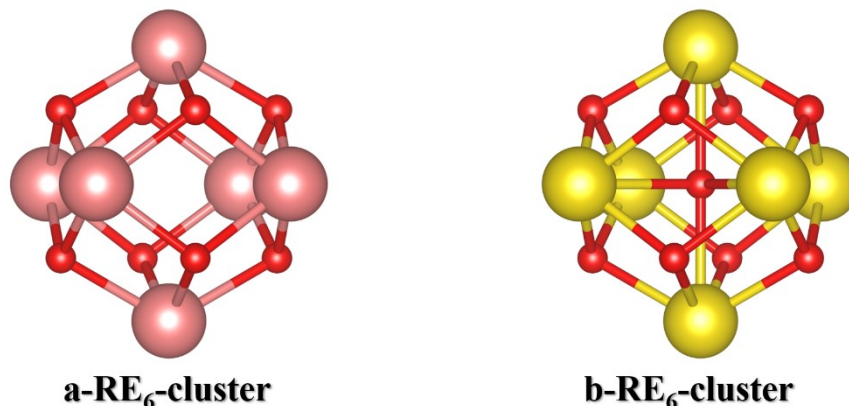
Figure 3.1. Schematic representation of the RE$_6$-hexanuclear cluster without the interstitial μ_6-O (left), and with it (right)

Recently, our group was able to synthesise microcrystalline powders of RE-UiO-66 (RE = Y(III), Eu(III), Gd(III), Tb(III), Ho(III), Er(III), Tm(III), and Yb(III)) and obtain a single crystal structure for Tm-UiO-66.[172] These materials are isoreticular to Zr-UiO-66, likely presenting the type a-RE$_6$-cluster without a μ_6-O in the centre of the cluster.

Herein, we report the synthesis of single crystals of all these RE-UiO-66 analogues obtained through optimising reaction conditions. A systematic study is performed to understand the relationship between RE(III)-O bond lengths holding the cluster together, and those which join the clusters to the linkers to give the network structure. Furthermore, we correlate these findings with the thermal stability of the materials and analyse them in order to form a hypothesis regarding the difficulty with synthesising light lanthanoid RE-UiO-66 analogues.

3.2. Experimental Procedures

3.2.1. General Materials and Methods

All solvents and reagents were purchased from commercial sources. N,N-dimethylacetamide (DMA), was purchased from Fisher Scientific (Fisher Chemical). Y(NO$_3$)$_3$·6H$_2$O, Eu(NO$_3$)$_3$·6H$_2$O, Gd(NO$_3$)$_3$·xH$_2$O, Tb(NO$_3$)$_3$·xH$_2$O, Ho(NO$_3$)$_3$·xH$_2$O, Er(NO$_3$)$_3$·xH$_2$O, Tm(NO$_3$)$_3$·xH$_2$O, Yb(NO$_3$)$_3$·xH$_2$O, and formic acid (HCOOH) were purchased from Alfa Aesar. 2,6-difluorobenzoic acid (2,6-DFBA) was purchased from Combi-Blocks. 1,4-

benzenedicarboxylic acid (H$_2$BDC) was purchased from Acros Organics. NMR solvents D$_2$SO$_4$ and DMSO-d$_6$ were purchased from Alfa Aesar. All solvents and chemicals were used without further treatment.

3.2.1.1. Single Crystal X-ray Diffraction

In all instances, measurements were carried out at 273 K or 298 K. The crystals diffracted weakly at high angles. Structure solutions were carried out using the SHELXTL package from Bruker,[161] and the parameters were refined using the OLEX2 software. All of the nonhydrogen atoms were refined with anisotropic thermal parameters. Hydrogen atoms were placed in calculated positions and allowed to ride on the carrier atoms.

An octahedral crystal from each vial was selected and mounted for X-ray diffraction data collection. The data for Y-, Eu-, Gd-, Tb-, and Er-UiO-66 was collected using a Bruker D8 Venture diffractometer equipped with a Photon 200 area detector, and IµS microfocus X-ray source (Bruker AXS, CuKα source).

The data for Ho-, Tm-, and Yb-UiO-66 was collected using a Bruker APEX-DUO diffractometer equipped with an APEX II CCD area detector, and IµS microfocus X-ray source (Bruker AXS, CuKα source).

It should be noted that disordered molecules (water, DMA, and dimethylammonium) in the MOF pores, which could not be reliably modelled using discrete atoms, were subtracted by SQUEEZE, using the PLATON software.

3.2.2. Y-, Eu-, Gd-, Tb-, Ho-, Er-, Tm-, and Yb-UiO-66 Synthesis

The products were obtained using solvothermal synthetic conditions in N,N-dimethylacetamide (DMA), with the aid of formic acid (HCOOH) 97% as a co-modulator at high temperatures (i.e., 140 °C or 150 °C). In a typical synthesis, 14 mg of the RE nitrate hydrate (11 mg for Y) are mixed with 7 mg of H$_2$BDC in 4 mL of a DMA:HCOOH mixture (**Table 3.1**) in a 6-dram vial. The vial is placed in a gravity convection oven at 140 °C (Eu) or 150 °C for approximately 4 days. Once the solvent mixture is nearly evaporated, octahedral crystals of varying size for each RE-UiO-66 analogue are observed growing on the walls of the vials (**Figure 3.2**). Using this procedure, not all the samples produced are phase pure as different morphologies are observed by optical microscopy. When Eu-UiO-66 was synthesised at 150 °C, the crystals

were much bigger than the ones grown at 140 °C, but of poor quality (**Figure 3.2d**), making their refinement not reliable.

Table 3.1. Solvent ratios used to obtain suitable structures for all the RE-UiO-66.

RE	*DMA:HCOOH*[a]
Y	3:1
Eu	2.5:1.5
Gd	3:1
Tb	2:2
Ho	3:2
Er	3:1
Tm	3:1
Yb	2:2

a. Variation of these ratios might affect the size of the crystals or amount of impurities found in them. For example, Tb-UiO-66 can also be obtained with a ratio of 3:1 yielding smaller crystals than 2:2.
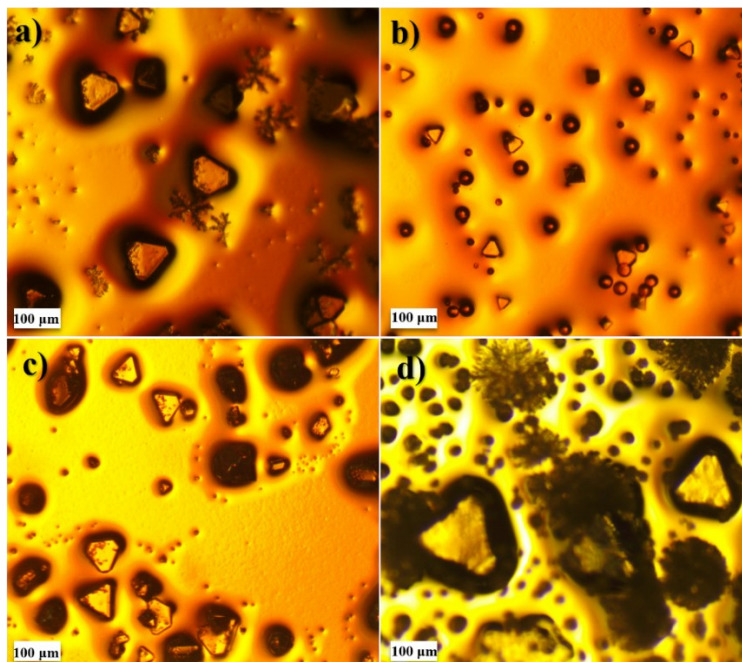
Figure 3.2. Optical microscope images of single crystals of (a) Ho-UiO-66, (b) Gd-UiO-66, and (c) Y-UiO-66, as well as (d) crystals of potential Eu-UiO-66 with scarce diffraction. The white box is 100 μm.

3.3. Results and Discussion

3.3.1. Structural Analysis

Similar to the previously reported Tm-UiO-66,[172] the crystal structures of all RE-UiO-66 analogues were solved in a cubic system, space group *Fm-3m* (**Table A.2**). In all cases there is only one crystallographically independent RE atom coordinated to four μ_3-OH from the RE_6-cluster and four O from the ligand COO$^-$ groups in a square antiprismatic fashion (**Figure 3.3**). Additionally, in the case of Eu-UiO-66 there is a ninth coordinated O with an occupancy factor of 0.4 giving rise to a capped square antiprismatic geometry (**Figure 3.3**). This O was left in that position to signal the existence of an extra coordinated molecule, like water, but its identity could not be resolved effectively. In literature examples of type b-RE_6 clusters with a μ_6-O at the centre of the cluster, significant electronic density should be observed in that position, which is not seen for the RE-UiO-66 series.[149] Although the bridging μ_3-OH atoms in the cluster do not show electron density that can be assigned to H, these are assumed to be μ_3-OH groups on the basis of charge neutrality of the framework.[29,67,149,164] In light of charge balancing, the RE_6-clusters present the formula $[RE_6(\mu_3\text{-OH})_8]^{10+}$. From the structure refinements it is observed that each cluster is connected to 12 BDC^{2-} linkers, where one half of each linker is associated with the cluster and the other half with a neighbouring cluster, so the overall charge of the framework is -2 (+10-12), requiring a counterion to balance the charge. DMA, when heated up, undergoes degradation to form acetate, and $[(CH_3)_2NH_2]^+$,[15] the latter of which can act as the counterion to achieve charge neutrality. Furthermore, if the bridging μ_3-OH were instead μ_3-O, then there should be a mixture of BDC^{2-} and $HBDC^-$ in the structure, each coordinating with different coordination modes. Since no such mixture of modes is found in the crystal structure, this further suggests that the bridging oxygen ligands are μ_3-OH rather than μ_3-O.
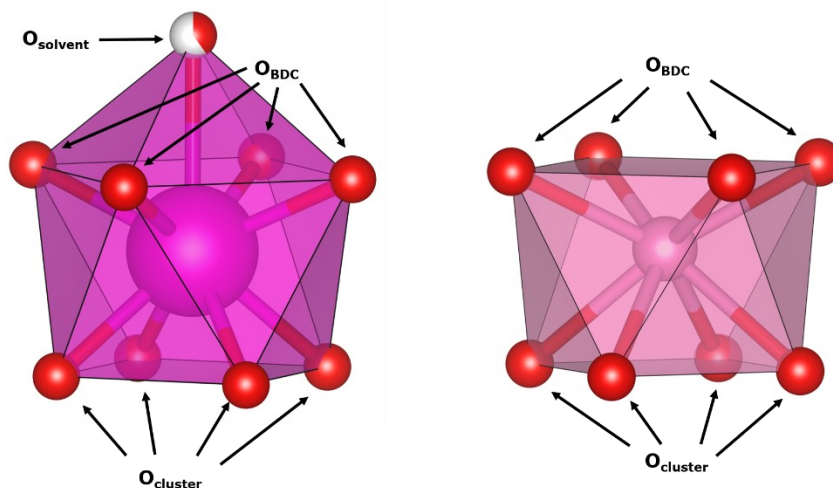
Figure 3.3. Representation of the two types of coordination environments found around the RE-ions for Eu (left), and the rest of the series (right).

3.3.2. Observed trends

When analysing the crystallographic data for each of the RE-UiO-66 analogues, the clearest trend is in the size of the unit cell parameter, *a*, which increases in size from the lighter RE elements to the heavier ones (**Table A.2**). It must be noted that Y(III), although a RE, does not possess *f*-electrons meaning slight off-trend behaviours can sometimes be expected.

As a first step to analysing the structures, the d(RE—COO) (**Figure 3.4a**); and d(RE—μ_3-OH) (**Figure 3.4b**) bond lengths were examined. As hypothesised, the RE-UiO-66 analogues present a trend regarding the bond distances between the metal ions and the oxygens from the cluster, d(RE—μ_3-OH); and the BDC linker, d(RE—COO) (**Figure 3.5a**). All the RE ions in RE-UiO-66 show a coordination number (CN) of 8, except for Eu, which seems to have, on average, 2.4 Eu ions per hexanuclear cluster with CN 9. A more frequent CN > 8 is expected for Eu-UiO-66 according to literature accounts on Eu-carboxylate compounds in which a larger proportion of molecules with CN 9 are observed in comparison to what is observed for heavier lanthanoids and Y.[175] Nonetheless, with the purpose of reducing the number of variables involved while analysing trends in the data, the CN of the Eu ions in Eu-UiO-66 is treated as 8.
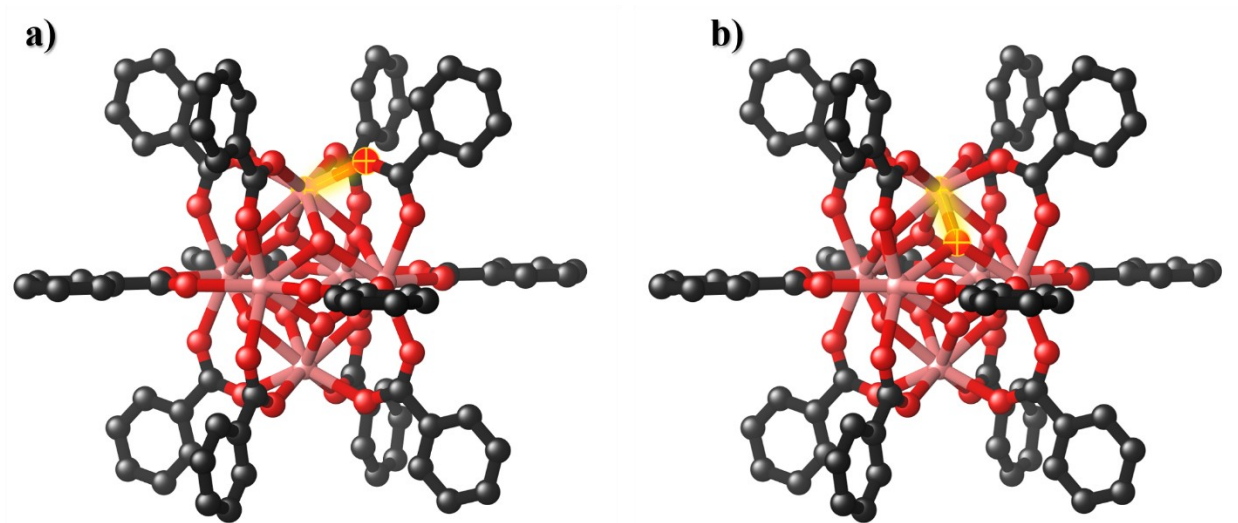
Figure 3.4. RE-UiO-66 SBU highlighting: (a) RE—COO, and (b) RE— μ_3-OH; in yellow.

When d(RE—μ_3-OH) vs. ionic radius is plotted, it can be readily observed that the value increases as the ionic radius, *r*, of the RE ion gets larger from Yb(III) to Eu(III) (**Figure 3.5a**). Such an increase in bond length is partially expected, since *r* itself is larger. But upon plotting Δ(RE—μ_3-OH) = d(RE— μ_3-OH) – *r*, CN = 8, what is observed is that the Δ(RE—μ_3-OH) is almost independent of the RE element (R^2 = 0.083) (**Figure 3.5b**).
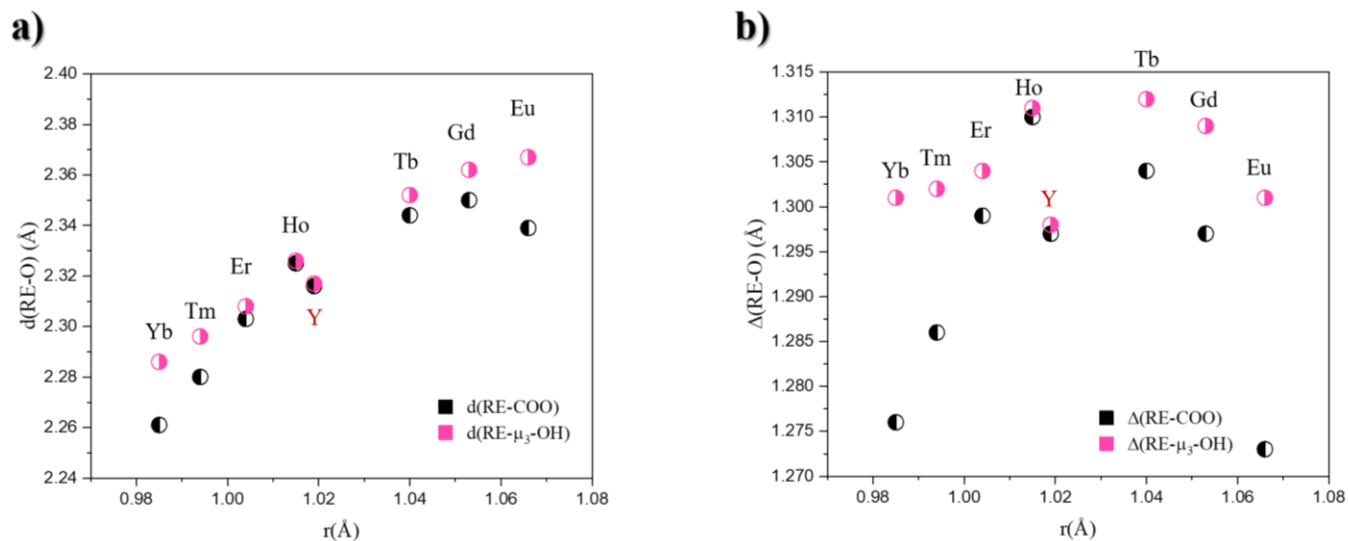
Figure 3.5. Plots showing (**a**) d(RE—O), and (**b**) Δ(RE—O). The pink symbols indicate a RE— μ_3-OH, while the black ones represent RE—COO. Y is marked red.

The d(RE—COO) for all RE-UiO-66 analogues are within the expected average range for RE compounds with bridging carboxylates as listed in **Table 3.2**, according to the thorough analysis made by Janicki *et al.*[175] When analysing Δ(RE—COO) = d(RE—COO) – r, CN = 8, it can be observed that the Δ(RE-COO) has more variation among the different RE-UiO-66 (**Figure 3.5b**). As the radius of the ion increases from Yb to Ho, so does the bond length between the carboxylate and the metal, reaching a maximum at Ho-UiO-66, after which the bond length begins decreasing again from Ho to Eu.

Table 3.2. Comparison between the average RE-carboxylate distances for all RE-compounds reported in the literature with CN 8 (in Å), and the ones obtained in this work in RE-UiO-66 (in Å).

RE	Experimental d(RE-COO)	Literature average d(RE-COO)^a
Y	2.316	2.315 ± 0.058
Eu	2.339	2.367 ± 0.048
Gd	2.35	2.357 ± 0.049
Tb	2.344	2.338 ± 0.046
Ho	2.325	2.317 ± 0.050
Er	2.303	2.306 ± 0.054
Tm	2.280	2.285 ± 0.057
Yb	2.261	2.289 ± 0.058

a. Values extracted from the work by Janicki *et al.*[175]

3.3.3. Effects on Stability

Based on our previous reports on RE-UiO-66, thermogravimetric analysis reveals that the decomposition temperature for RE-UiO-66 analogues to their respective RE(III) oxides occurs at temperatures of ~560 °C (Y), ~555 °C (Tm and Yb), ~558 °C (Er), ~551 °C (Tb), and ~505 °C (Eu).[172] Eu-UiO-66 exhibits a markedly lower decomposition temperature, being *ca*. 50 °C less than the other RE-UiO-66 analogues. In addition, Eu-UiO-66 proved to be the most difficult RE-UiO-66 analogue to synthesise, often with the lowest crystalline quality of the series.[172] There are two aspects to the structure of Eu-UiO-66 that should be noted: i) Eu-UiO-66 shows the largest absolute difference between Δ(RE—COO) and Δ(RE—μ_3-OH) (**Figure 3.6**), slightly larger than

that of Yb-UiO-66; ii) Eu-UiO-66 is the only structure showing a portion of Eu(III) ions with a CN of 9. It is likely that the formation of other Eu-BDC coordination compounds is favoured over the formation of Eu-UiO-66 due to the strength of the RE—COO bond being higher than the Eu—μ_3-OH bond of the cluster node. Furthermore once Eu-UiO-66 is formed, we hypothesise that some of the 8-coordinated Eu(III) ions in the cluster are more susceptible to attack from neutral coordinating ligands like water, making the framework less stable overall than the other RE-UiO-66 analogues. While it is true that Yb-, and Tm-UiO-66 also show a relatively large gap between the Δ(RE—COO) and Δ(RE—μ_3-OH) bond lengths, these two rare earth elements do not have a preference to be 9-coordinated.
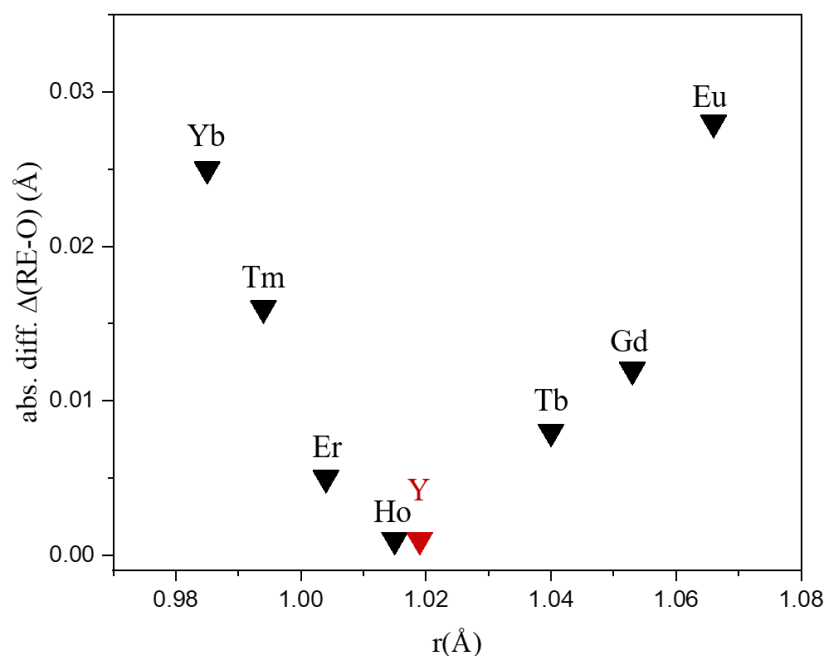
Figure 3.6. Absolute difference between Δ(RE—COO) and Δ(RE—μ_3-OH) showing a minimum for the middle lanthanoids from the series and Y. Y is marked red.

To determine if the same trend is observed in other MOFs with **fcu** topology, the series of M(IV)-UiO-66 (M = Zr, Ce, and Th) was analysed in the same way using their reported crystal structures (**Figure 3.7**).[53,60,61] Thermogravimetric analysis shows both Ce(IV)-UiO-66 and Th(IV)-UiO-66 have decomposition temperatures of 240 °C and 420 °C which are lower than that of Zr(IV)-UiO-66 (550 °C) and the RE-UiO-66 analogues. Ce(IV) and Th(IV)-UiO-66 also both present a longer d(M—COO) than d(M—μ_3-O) (here the character of the bridging O is a mixture of μ_3-O and μ_3-OH), which is the opposite of what is observed for Zr(IV)-UiO-66 and the RE-

UiO-66 analogues. We therefore hypothesise that the lower decomposition temperature of the *f*-block based M(IV)-UiO-66 comes partly from the inversion of the bond distances between the ions to the linkers *vs.* the cluster. Moreover, Ce(IV)-UiO-66 has a much lower decomposition temperature than the other two M(IV)-UiO-66. This can be explained by its Δ(Ce(IV)—COO) being abnormally high for the ionic radius of Ce(IV), which might suggest that the strength of the bond between Ce(IV) and the BDC linker is not as high as that observed for Zr-, and Th-UiO-66. It must be noted here that the crystal structure of Th-UiO-66 unambiguously shows that all the Th ions have a CN 9,[61] so that is taken into account when determining the radius to use for the analysis. In the series of M(IV)-UiO-66 and RE(III)-UiO-66, the differences between decomposition temperatures among the isoreticular structures are thus hypothesised to come from different phenomena.

This all points to the following: the thermal (and potentially chemical) stability of MOFs with **fcu** topology, and possibly all cluster-based MOFs by extension, are affected by i) the relationship between Δ(M—COO) and Δ(M—μ_3-O). In this sense, when Δ(M—COO) > Δ(M—μ_3-O) and the difference between these two is relatively high, the thermal stability of the MOF is diminished.
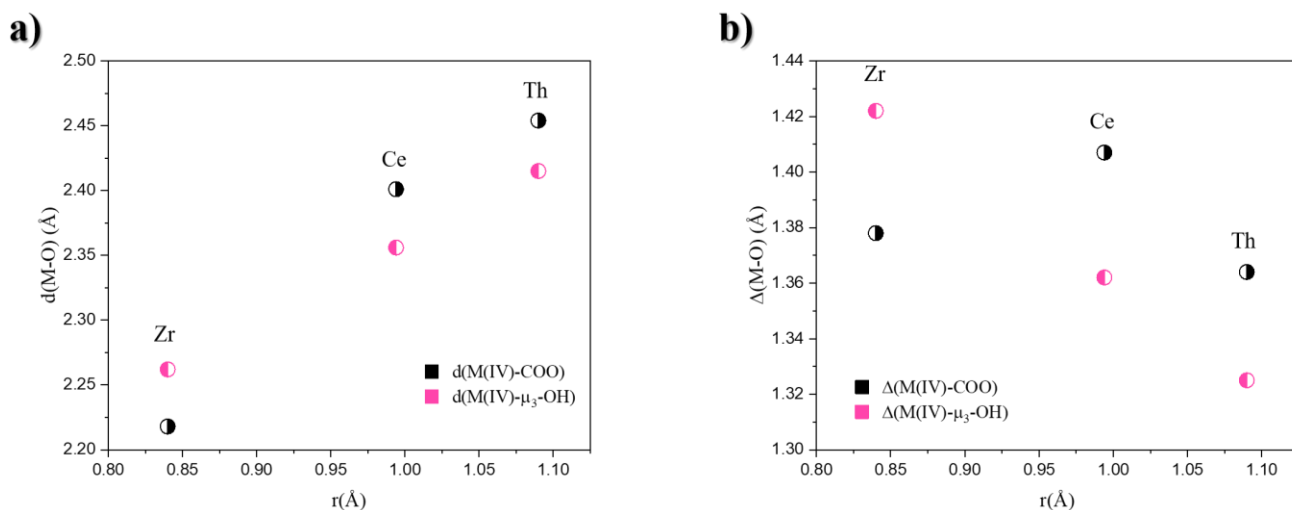
Figure 3.7. Plots showing (a) d(M(IV)—O), and (b) Δ(M(IV)—O). The pink symbols indicate a M—μ_3-O, while the black ones represent M—COO.

Another observation, this time towards the heavier lanthanoids Tm and Yb, is regarding the formation of impurities during their synthesis (**Figure 3.8**). Tm-UiO-66 and Yb-UiO-66,

although not requiring DMA for synthesis, are more susceptible to the batch of DMF used than Y-UiO-66 and Er-UiO-66 and often require HNO_3 to be synthesised. The Tm—COO, and Yb—COO bonds are considerably shorter than the corresponding RE—μ_3-OH, which might explain why other secondary phases tend to form during the synthesis of these MOFs. Under the conditions used in this work, for example, it can be seen that the Er-sample contains impurities, but UiO-66 can be observed nonetheless, whereas the Tm-sample shows barely any peak for UiO-66 (**Figure 3.9**). If the RE$_6$-cluster does not have enough time to form before the BDC linker coordinates to the ions, then it is more likely that RE-coordination compounds or RE-coordination polymers will form.
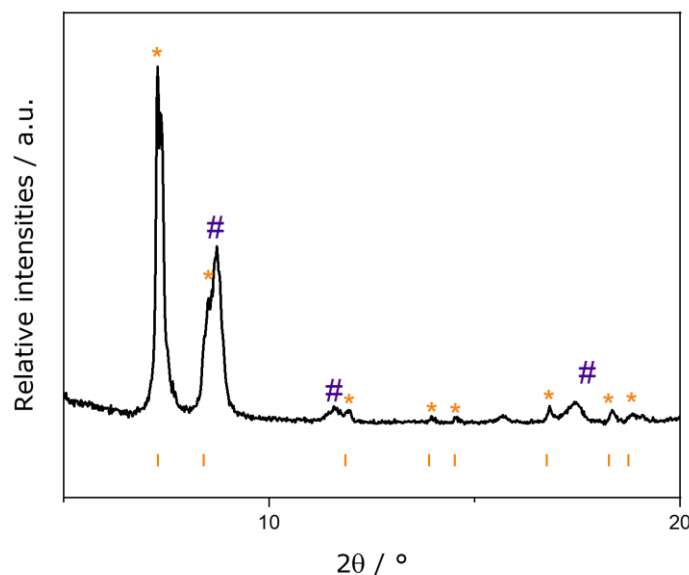
Figure 3.8. Example of a PXRD diffractogram of a Yb-sample containing Yb-UiO-66 (marked with orange *) and an unknown phase (marked with purple #) under previously reported synthesis conditions.[172]
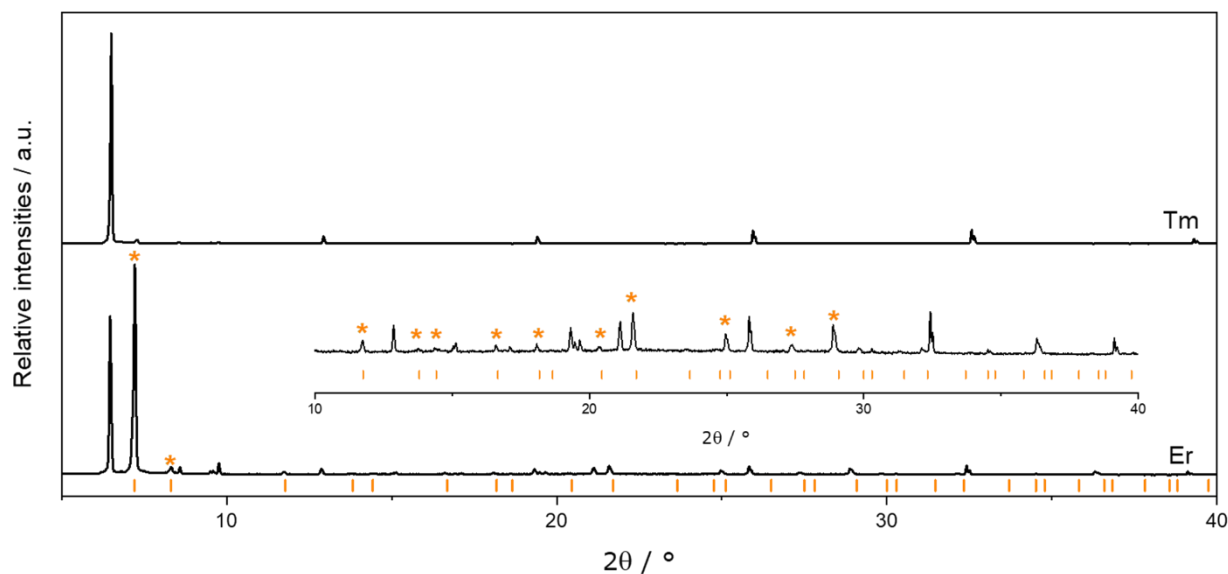
Figure 3.9. PXRD diffractograms of the crystal samples collected for Tm (top) and Er (bottom).

Attempts to synthesise early lanthanoid UiO-66 analogues — La(III), Ce(III), Pr(III), and Nd(III) — or Lu(III)-UiO-66, using the synthetic protocols developed in this thesis, or slight modifications of it, have been unsuccessful. We hypothesise that the difference between Δ(RE—COO) and Δ(RE—μ_3-OH) will continue to increase as r grows larger (towards La(III)), or smaller (towards Lu(III)), and thus the materials become more difficult to precipitate under these conditions, similar to what is already observed for Eu-, Tm-, and Yb-UiO-66 but more accentuated. It still remains a mystery whether the interstitial μ_6-O might be pivotal to stabilise the cluster of the larger RE ions or how it might affect these trends, or even if it is possible to synthesise these other RE-UiO-66 analogues. In agreement with this analysis, the best quality crystals, and most robust MOFs, were obtained from those REs which show a minimum difference between Δ(RE—COO) and Δ(RE—μ_3-OH) — Ho-, and Y-UiO-66.

3.3.4. The Effects of Temperature on Crystal Quality

From these crystallisation experiments it was noticed that contrary to conventional crystal growth procedures, higher temperatures yielded larger crystals, suitable for SCXRD. There are two phases that can be identified in the crystal formation process: i) nucleation, and ii) growth. These two processes can happen simultaneously during crystal formation, each having their own

thermodynamic rate.[171] For MOFs it has been found that these two phases have similar rates which explains why these materials tend to form crystalline powders rather than single crystals. Likely in our case, the faster evaporation of the solvent as the temperature nears its boiling point (165 °C for DMA) pushes the system towards a non-equilibrium state which favours the growth of the few formed nuclei into well-defined single crystals. Adversely, as a consequence of this forced growth, sometimes the crystals can grow to a large size without giving the structure time to correct mistakes and crystallise in an orderly fashion.

In Eu-UiO-66, the system can grow imperfectly hindering the crystal quality as temperature is increased. When Eu-UiO-66 was synthesised at 150 °C, we obtained the largest possible crystals (*ca.* 200 µm) as a consequence of fast-induced growth but the crystals show rather poor diffraction at high angles and sometimes signs of polycrystallinity (multiple domains growing inside the same crystal). Furthermore, these crystals were brittle enough to be easily shattered under slight pressure with a metal spatula. On the contrary, when the same synthetic conditions were used at 140 °C, the quality of the material improved enough to be able to obtain a structure by SCXRD analysis.

3.5. Conclusions

A protocol to obtain single crystals of the family of RE-UiO-66 analogues suitable for SCXRD has been presented and their crystal structures analysed and studied. It is confirmed that the entire family of RE-UiO-66 presents an a-type RE_6-cluster in line with similar structures presented in other studies in the literature. A feasible explanation for the thermal stability trends of the RE-UiO-66 was presented from a structure analysis, showing why Eu-UiO-66 seems to be less stable than the rest of the family, and the stability trends of RE-UiO-66 were compared to the M(IV)-UiO-66 analogues. Additionally, the difference between Δ(RE—COO) and Δ(RE—μ_3-OH) was used to explain the difficulties in synthesising suitable crystals from the extremes of the rare earth element series — Eu-UiO-66, and Yb- and Tm-UiO-66 — and address the apparent challenges associated with synthesising RE-UiO-66 analogues using La(III), Ce(III), Pr(III), Nd(III), and Lu(III). Finally, observations regarding the crystal quality of Eu-UiO-66, being related to a delicate balance between crystal nucleation and growth, was discussed.

Chapter 4
Conclusions and Future Work

4.1. General Conclusions

The lack of RE-UiO-66 analogues in the literature drew our attention due to this type of structure being the simplest and most well-studied Zr-hexanuclear cluster-based MOF. We have optimised and described for the first time a protocol that utilises the fluorinated modulator 2,6-DFBA, together with H_2BDC and $RE(NO_3)_3 \cdot H_2O$, to produce a MOF with RE(III)-hexanuclear clusters bridged together by linear linkers, called RE-UiO-66. RE-UiO-66 is isostructural to the archetypical Zr-UiO-66. A large family of RE-UiO-66 analogues [RE = Y(III), Eu(III), Gd(III), Tb(III), Ho(III), Er(III), Tm(III), and Yb(III)] was synthesised, isolated, activated, and characterised. RE-UiO-66 was found to have surface area and porosity similar to that of Zr-UiO-66 while presenting similar PXRD diffractograms, and DRIFTS and ^{1}H-NMR spectrograms. Although the RE-UiO-66 series shows promising properties, it was discovered that it is not as structurally stable upon activation or aging as Zr-UiO-66 according to the regular procedures used in the MOF field. In chapter 2 we presented this detailed characterisation, and analysis, together with a series of steps to troubleshoot the synthesis of the different RE-UiO-66.

A more detailed structural study is needed to understand the reasons behind the lack of success in synthesising larger RE-UiO-66 with larger lanthanoids [La(III) to Nd (III)]. In order to do this, in chapter 3 we optimised the conditions to grow single crystals of the RE-UiO-66 suitable for SCXRD and performed a systematic analysis on the parameters obtained from the refinements. We correlated the trends found with the difficulty in synthesising certain RE-UiO-66 [RE(III) = Eu(III), Gd(III), and Tb(III)], and the sensitivity of the reaction to the parameters employed [RE(III) = Tm(III), and Yb(III)]. We also hypothesised that the reason behind the difficulties in the synthesis of earlier and later lanthanoids might be related to the expansion of these trends towards the extremes of the series.

4.2. Future Work

In the interest of completing a systematic analysis of RE-UiO-66 for the whole series of lanthanoids, efforts should concentrate on the development of a synthetic protocol for La(III)-UiO-66, Ce(III)-UiO-66, Pr(III)-UiO-66, Nd(III)-UiO-66, Sm(III)-UiO-66, Dy(III)-UiO-66, and Lu(III)-UiO-66. An analysis of the bond distances in the whole series might shed more light on the correlation between these bond lengths and the structural stability or other chemical properties of these materials. Furthermore, similar analysis should be done across other RE-hexanuclear cluster containing **fcu** structures to corroborate whether the trends observed for the synthesised RE-UiO-66 series are transferrable to other systems or if they are intrinsic to this structure alone. Such an analysis spanning the whole series of lanthanoids, in cluster containing RE-MOF, has not as of yet been done.

In the same line of thought, the possibility of synthesising similar structures containing the b-RE(III)$_6$-cluster should be contemplated. This **fcu** MOF, if able to be synthesised would surely prove to have different properties than the ones containing a-RE(III)$_6$-clusters.

While the RE-UiO-66 family shows promising properties for some applications, the problem of its relatively lower stability should be further probed in order to understand the reasons behind it. Stabilisation of the structure could be achieved *via* incorporation of templating species inside of the pores of the MOFs, or *via* cation exchange which will render a non-organic counterion inside the structure, not able to escape under vacuum activation conditions. Other, milder activation procedures could be tested on the material to ensure the structure is not exposed to high thermal stress. Furthermore, a study on the stability of RE-UiO-66 should be done in order to correctly assess its potential uses. A complete study on stability would entail testing the robustness of the RE-UiO-66 against i) aqueous and organic media, ii) basic and acidic pH, iii) phosphate buffer, and iv) against redox agents that could cause the collapse, or phase transition, of the structure. An increased stability for the RE-UiO-66 family would encourage their use in catalytic applications while taking advantage of the Lewis acid sites inherently present in the structure. In particular, catalysis in aqueous media is of interest as RE-UiO-66 could be used to degrade water contaminants.

References

1   B. F. Hoskins and R. Robson, *J. Am. Chem. Soc.*, 1989, **111**, 5962–5964.

2   O. M. Yaghi and H. Li, *J. Am. Chem. Soc.*, 1995, **117**, 10401–10402.

3   O. M. Yaghi, G. Li and H. Li, *Nature*, 1995, **378**, 703–706.

4   H. Li, M. Eddaoudi, M. O'Keeffe and O. M. Yaghi, *Nature*, 1999, **402**, 276–279.

5   M. Kondo, T. Yoshitomi, H. Matsuzaka, S. Kitagawa and K. Seki, *Angew. Chem. Int. Ed.*, 1997, **36**, 1725–1727.

6   A. K. Cheetham, G. Férey and T. Loiseau, *Angew. Chem. Int. Ed.*, 1999, **38**, 3268–3292.

7   N. L. Rosi, J. Kim, M. Eddaoudi, B. Chen, M. O'Keeffe and O. M. Yaghi, *J. Am. Chem. Soc.*, 2005, **127**, 1504–1518.

8   N. Joseph, H. D. Lawson, K. J. Overholt, K. Damodaran, R. Gottardi, A. P. Acharya and S. R. Little, *Sci. Rep.*, 2019, **9**, 1–11.

9   L. Robison, L. Zhang, R. J. Drout, P. Li, C. R. Haney, A. Brikha, H. Noh, B. L. Mehdi, N. D. Browning, V. P. Dravid, Q. Cui, T. Islamoglu and O. K. Farha, *ACS Appl. Bio Mater.*, 2019, **2**, 1197–1203.

10 G. Férey, M. Latroche, C. Serre, F. Millange, T. Loiseau and A. Percheron-Guégan, *Chem. Commun.*, 2003, 2976–2977.

11 K. Otake, Y. Cui, C. T. Buru, Z. Li, J. T. Hupp and O. K. Farha, *J. Am. Chem. Soc.*, 2018, **140**, 8652–8656.

12 D. Feng, Z.-Y. Gu, J.-R. Li, H.-L. Jiang, Z. Wei and H.-C. Zhou, *Angew. Chem. Int. Ed.*, 2012, **51**, 10307–10310.

13 D. Feng, K. Wang, Z. Wei, Y.-P. Chen, C. M. Simon, R. K. Arvapally, R. L. Martin, M. Bosch, T.-F. Liu, S. Fordham, D. Yuan, M. A. Omary, M. Haranczyk, B. Smit and H.-C. Zhou, *Nat. Commun*, 2014, **5**, 1–9.

14 A. Phan, C. J. Doonan, F. J. Uribe-Romo, C. B. Knobler, M. O'Keeffe and O. M. Yaghi, *Acc. Chem. Res.*, 2010, **43**, 58–67.

15 D.-X. Xue, A. J. Cairns, Y. Belmabkhout, L. Wojtas, Y. Liu, M. H. Alkordi and M. Eddaoudi, *J. Am. Chem. Soc.*, 2013, **135**, 7660–7667.

16 E. A. Dolgopolova, A. M. Rice and N. B. Shustova, *Chem. Commun.*, 2018, **54**, 6472–6483.

17 S. L. Hanna, X. Zhang, K. Otake, R. J. Drout, P. Li, T. Islamoglu and O. K. Farha, *Cryst. Growth Des.*, 2019, **19**, 506–512.

18 H. Furukawa, K. E. Cordova, M. O'Keeffe and O. M. Yaghi, *Science.*

19 S. R. Batten, N. R. Champness, X.-M. Chen, J. Garcia-Martinez, S. Kitagawa, L. Öhrström, M. O'Keeffe, S. M. Paik and J. Reedijk, *Pure and Applied Chemistry*, 2013, **85**, 1715–1724.

20 S. R. Batten, N. R. Champness, X.-M. Chen, J. Garcia-Martinez, S. Kitagawa, L. Öhrström, M. O'Keeffe, M. P. Suh and J. Reedijk, *CrystEngComm*, 2012, **14**, 3001–3004.

21 H. Furukawa, N. Ko, Y. B. Go, N. Aratani, S. B. Choi, E. Choi, A. O. Yazaydin, R. Q. Snurr, M. O'Keeffe, J. Kim and O. M. Yaghi, *Science*, 2010, **329**, 424–428.

22 Hönicke, I. M.; Senkovska, I.; Bon, V.; Baburin, I. A.; Bönisch, N.; Raschke, S.; Evans, J. D.; Kaskel, S. *Angew. Chem. Int. Ed.,* 2018, **57** (42), 13780–13783.

23 Z. Chen, P. Li, R. Anderson, X. Wang, X. Zhang, L. Robison, L. R. Redfern, S. Moribe, T. Islamoglu, D. A. Gómez-Gualdrón, T. Yildirim, J. F. Stoddart and O. K. Farha, *Science*, 2020, **368**, 297–303.

24 P. Li, N. A. Vermeulen, C. D. Malliakas, D. A. Gómez-Gualdrón, A. J. Howarth, B. L. Mehdi, A. Dohnalkova, N. D. Browning, M. O'Keeffe and O. K. Farha, *Science*, 2017, **356**, 624–627.

25 Y. Bai, Y. Dou, L.-H. Xie, W. Rutledge, J.-R. Li and H.-C. Zhou, *Chem. Soc. Rev.*, 2016, **45**, 2327–2367.

26 S. Barthel, E. V. Alexandrov, D. M. Proserpio and B. Smit, *Crys. Growth Des.*, 2018, **18**, 1738–1747.

27 J. A. Mason, M. Veenstra and J. R. Long, *Chem. Sci.*, 2013, **5**, 32–51.

28 S. Ma and H.-C. Zhou, *J. Am. Chem. Soc.*, 2006, **128**, 11734–11735.

29 D.-X. Xue, Y. Belmabkhout, O. Shekhah, H. Jiang, K. Adil, A. J. Cairns and M. Eddaoudi, *J. Am. Chem. Soc.*, 2015, **137**, 5034–5040.

30 J. Lee, O. K. Farha, J. Roberts, K. A. Scheidt, S. T. Nguyen and J. T. Hupp, *Chem. Soc. Rev.*, 2009, **38**, 1450–1459.

31 D. Yang and B. C. Gates, *ACS Catal.*, 2019, **9**, 1779–1798.

32 C. Wang, B. An and W. Lin, *ACS Catal.*, 2019, **9**, 130–146.

33 L. E. Kreno, K. Leong, O. K. Farha, M. Allendorf, R. P. Van Duyne and J. T. Hupp, *Chem. Rev.*, 2012, **112**, 1105–1125.

34 C. A. Bauer, T. V. Timofeeva, T. B. Settersten, B. D. Patterson, V. H. Liu, B. A. Simmons and M. D. Allendorf, *J. Am. Chem. Soc.*, 2007, **129**, 7136–7144.

35 Howarth, A. J.; Liu, Y.; Hupp, J. T.; Farha, O. K. *CrystEngComm.,* 2015, **17** (38), 7245–7253.

36 Drout, R. J.; Robison, L.; Chen, Z.; Islamoglu, T.; Farha, O. K. *Trends Chem.,* 2019, **1** (3), 304–317.

37 P. A. Kobielska, A. J. Howarth, O. K. Farha and S. Nayak, *Coord. Chem. Rev.*, 2018, **358**, 92–107.

38 Li, B.; Wen, H.-M.; Cui, Y.; Zhou, W.; Qian, G.; Chen, B. *Adv. Mater.,* 2016, **28** (40), 8819–8860.

39 C. Pagis, M. Ferbinteanu, G. Rothenberg and S. Tanase, *ACS Catal.*, 2016, **6**, 6063–6072.

40 F. Saraci, V. Quezada-Novoa, P. R. Donnarumma and A. J. Howarth, *Chem. Soc. Rev.*, 2020, **49**, 7949–7977.

41 M. Seitz, A. G. Oliver and K. N. Raymond, *J. Am. Chem. Soc.*, 2007, **129**, 11153–11160.

42 H. Jiang, J. Jia, A. Shkurenko, Z. Chen, K. Adil, Y. Belmabkhout, L. J. Weselinski, A. H. Assen, D.-X. Xue, M. O'Keeffe and M. Eddaoudi, *J. Am. Chem. Soc.*, 2018, **140**, 8858–8867.

43 D. Alezi, A. M. P. Peedikakkal, Ł. J. Weseliński, V. Guillerm, Y. Belmabkhout, A. J. Cairns, Z. Chen, Ł. Wojtas and M. Eddaoudi, *J. Am. Chem. Soc.*, 2015, **137**, 5421–5430.

44 S. Fordham, X. Wang, M. Bosch and H.-C. Zhou, in *Lanthanide Metal-Organic Frameworks*, ed. P. Cheng, Springer Berlin Heidelberg, Berlin, Heidelberg, 2014, vol. 163, pp. 1–27.

45 O. M. Yaghi, M. O'Keeffe, N. W. Ockwig, H. K. Chae, M. Eddaoudi and J. Kim, *Nature*, 2003, **423**, 705–714.

46 O. M. Yaghi, *J. Am. Chem. Soc.*, 2016, **138**, 15507–15509.

47 O. M. Yaghi, *ACS Cent. Sci.*, 2019, **5**, 1295–1300.

48 M. O'Keeffe, M. A. Peskov, S. J. Ramsden and O. M. Yaghi, *Acc. Chem. Res.*, 2008, **41**, 1782–1789.

49 L. Öhrström, *Crystals*, 2015, **5**, 154–162.

50 J. Winarta, B. Shan, S. M. Mcintyre, L. Ye, C. Wang, J. Liu and B. Mu, *Crys. Growth Des.*, 2020, **20**, 1347–1362.

51 J. H. Cavka, S. Jakobsen, U. Olsbye, N. Guillou, C. Lamberti, S. Bordiga and K. P. Lillerud, *J. Am. Chem. Soc.*, 2008, **130**, 13850–13851.

52 M. J. Katz, Z. J. Brown, Y. J. Colón, P. W. Siu, K. A. Scheidt, R. Q. Snurr, J. T. Hupp and O. K. Farha, *Chem. Commun.*, 2013, **49**, 9449–9451.

53 Trickett, C. A.; Gagnon, K. J.; Lee, S.; Gándara, F.; Bürgi, H.-B.; Yaghi, O. M. *Angew. Chem. Int. Ed.,* 2015, **54** (38), 11162–11167.

54 A. Schaate, P. Roy, A. Godt, J. Lippke, F. Waltz, M. Wiebcke and P. Behrens, *Chem. Eur. J.*, 2011, **17**, 6643–6651.

55 Y. Zhao, Q. Zhang, Y. Li, R. Zhang and G. Lu, *ACS Appl. Mater. Interfaces*, 2017, **9**, 15079–15085.

56 L. Valenzano, B. Civalleri, S. Chavan, S. Bordiga, M. H. Nilsen, S. Jakobsen, K. P. Lillerud and C. Lamberti, *Chem. Mater.*, 2011, **23**, 1700–1718.

57 H. Wu, Y. S. Chua, V. Krungleviciute, M. Tyagi, P. Chen, T. Yildirim and W. Zhou, *J. Am. Chem. Soc.*, 2013, **135**, 10525–10532.

58 P. Ghosh, Y. J. Colón and R. Q. Snurr, *Chem. Commun.*, 2014, **50**, 11329–11331.

59 Z. Hu, A. Nalaparaju, Y. Peng, J. Jiang and D. Zhao, *Inorg. Chem.*, 2016, **55**, 1134–1141.

60 M. Lammert, M. T. Wharmby, S. Smolders, B. Bueken, A. Lieb, K. A. Lomachenko, D. D. Vos and N. Stock, *Chem. Commun.*, 2015, **51**, 12578–12581.

61 C. Falaise, J.-S. Charles, C. Volkringer and T. Loiseau, *Inorg. Chem.*, 2015, **54**, 2235–2242.

62 C. Falaise, C. Volkringer, J.-F. Vigier, N. Henry, A. Beaurain and T. Loiseau, *Chem. Eur. J.*, 2013, **19**, 5324–5331.

63 A. M. Hastings, D. Ray, W. Jeong, L. Gagliardi, O. K. Farha and A. E. Hixon, *J. Am. Chem. Soc.*, 2020, **142**, 9363–9371.

64 Z. Zheng, *Chem. Commun.*, 2001, 2521–2529.

65 R. Wang, H. Liu, M. D. Carducci, T. Jin, C. Zheng and Z. Zheng, *Inorg. Chem.*, 2001, **40**, 2743–2750.

66 R. Wang, H. D. Selby, H. Liu, M. D. Carducci, T. Jin, Z. Zheng, J. W. Anthis and R. J. Staples, *Inorg. Chem.*, 2002, **41**, 278–286.

67 G. Calvez, C. Daiguebonne, O. Guillou, T. Pott, P. Méléard and F. Le Dret, *Comptes Rendus Chimie*, 2010, **13**, 715–730.

68 Trickett, C. A.; Gagnon, K. J.; Lee, S.; Gándara, F.; Bürgi, H.-B.; Yaghi, O. M. Definitive Molecular Level Characterization of Defects in UiO-66 Crystals. *Angew. Chem. Int. Ed.,* 2015, **54** (38), 11162–11167.

69 V. Quezada-Novoa, H. M. Titi, A. Sarjeant and A. Howarth, 2020, DOI:10.26434/chemrxiv.12355406.v1.

70 Y. Zhang, L. Huang, H. Miao, H. X. Wan, H. Mei, Y. Liu and Y. Xu, *Chem. Eur. J.*, 2015, **21**, 3234–3241.

71 L.-F. Chen, J. Zhang, G.-Q. Ren, Z.-J. Li, Y.-Y. Qin, P.-X. Yin, J.-K. Cheng and Y.-G. Yao, *CrystEngComm*, 2008, **10**, 1088–1092.

72 C. Liu, S. V. Eliseeva, T.-Y. Luo, P. F. Muldoon, S. Petoud and N. L. Rosi, *Chem. Sci.*, 2018, **9**, 8099–8102.

73 D. F. Sava Gallis, L. E. S. Rohwer, M. A. Rodriguez, M. C. Barnhart-Dailey, K. S. Butler, T. S. Luk, J. A. Timlin and K. W. Chapman, *ACS Appl. Mater. Interfaces*, 2017, **9**, 22268–22277.

74 Y. Zhang, Y. Wang, L. Liu, N. Wei, M.-L. Gao, D. Zhao and Z.-B. Han, *Inorg. Chem.*, 2018, **57**, 2193–2198.

75 A. J. Howarth, A. W. Peters, N. A. Vermeulen, T. C. Wang, J. T. Hupp and O. K. Farha, *Chem. Mater.*, 2017, **29**, 26–39.

76 D. Feng, W.-C. Chung, Z. Wei, Z.-Y. Gu, H.-L. Jiang, Y.-P. Chen, D. J. Darensbourg and H.-C. Zhou, *J. Am. Chem. Soc.*, 2013, **135**, 17105–17110.

77 D. Feng, Z.-Y. Gu, Y.-P. Chen, J. Park, Z. Wei, Y. Sun, M. Bosch, S. Yuan and H.-C. Zhou, *J. Am. Chem. Soc.*, 2014, **136**, 17714–17717.

78 H.-L. Jiang, D. Feng, K. Wang, Z.-Y. Gu, Z. Wei, Y.-P. Chen and H.-C. Zhou, *J. Am. Chem. Soc.*, 2013, **135**, 13934–13938.

79 Y. Chen, S. Zhang, F. Chen, S. Cao, Y. Cai, S. Li, H. Ma, X. Ma, P. Li, X. Huang and B. Wang, *J. Mater. Chem. A*, 2018, **6**, 342–348.

80 H. Guo, Y. Zhu, S. Qiu, J. A. Lercher and H. Zhang, *Adv. Mater. Weinheim*, 2010, **22**, 4190–4192.

81 Al-Kutubi, H.; Gascon, J.; Sudhölter, E. J. R.; Rassaei, L. Electrosynthesis of Metal-Organic Frameworks: Challenges and Opportunities. *ChemElectroChem,* 2015, **2** (4), 462–474.

82 M. Li and M. Dincă, *J. Am. Chem. Soc.*, 2011, **133**, 12926–12929.

83 I. Huskić, M. Arhangelskis and T. Friščić, *Green Chem.*, 2020, **22**, 4364–4375.

84 Brekalo, Deliz, Kane, Friščić, and Holman, *Molecules*, 2020, **25**, 633.

85 Khan, N. A.; Jhung, S. H. *Coord. Chem. Rev.,* 2015, **285**, 11–23.

86 J. E. Efome, D. Rana, T. Matsuura and C. Q. Lan, *ACS Appl. Mater. Interfaces*, 2018, **10**, 18619–18629.

87 D. Alezi, Y. Belmabkhout, M. Suyetin, P. M. Bhatt, Ł. J. Weseliński, V. Solovyeva, K. Adil, I. Spanopoulos, P. N. Trikalitis, A.-H. Emwas and M. Eddaoudi, *J. Am. Chem. Soc.*, 2015, **137**, 13308–13318.

88 S. Yuan, L. Huang, Z. Huang, D. Sun, J.-S. Qin, L. Feng, J. Li, X. Zou, T. Cagin and H.-C. Zhou, *J. Am. Chem. Soc.*, 2020, **142**, 4732–4738.

89 B. Liu, A. G. Wong-Foy and A. J. Matzger, *Chem. Commun.*, 2013, **49**, 1419–1421.

90 T. K. Prasad and M. P. Suh, *Chem. Eur. J.*, 2012, **18**, 8673–8680.

91 X. Zhang, Z. Chen, X. Liu, S. L. Hanna, X. Wang, R. Taheri-Ledari, A. Maleki, P. Li and O. K. Farha, *Chem. Soc. Rev.*, 2020, **49**, 7406–7427.

92 L. Ma, A. Jin, Z. Xie and W. Lin, *Angew. Chem. Int. Ed.*, 2009, **48**, 9905–9908.

93 J. E. Mondloch, W. Bury, D. Fairen-Jimenez, S. Kwon, E. J. DeMarco, M. H. Weston, A. A. Sarjeant, S. T. Nguyen, P. C. Stair, R. Q. Snurr, O. K. Farha and J. T. Hupp, *J. Am. Chem. Soc.*, 2013, **135**, 10294–10297.

94 E. J. Lee, J. Bae, K. M. Choi and N. C. Jeong, *ACS Appl. Mater. Interfaces*, 2019, **11**, 35155–35161.

95 Y. Kalinovskyy, N. J. Cooper, M. J. Main, S. J. Holder and B. A. Blight, *Dalton Trans.*, 2017, **46**, 15704–15709.

96 Y. G. Chung, J. Camp, M. Haranczyk, B. J. Sikora, W. Bury, V. Krungleviciute, T. Yildirim, O. K. Farha, D. S. Sholl and R. Q. Snurr, *Chem. Mater.*, 2014, **26**, 6185–6192.

97 J. E. Mondloch, M. J. Katz, N. Planas, D. Semrouni, L. Gagliardi, J. T. Hupp and O. K. Farha, *Chem. Commun.*, 2014, **50**, 8944–8946.

98 Wilmer, C. E.; Leaf, M.; Lee, C. Y.; Farha, O. K.; Hauser, B. G.; Hupp, J. T.; Snurr, R. Q. Large-Scale Screening of Hypothetical Metal–Organic Frameworks. *Nature Chem.,* 2012, **4** (2), 83–89.

99 O. K. Farha, A. M. Shultz, A. A. Sarjeant, S. T. Nguyen and J. T. Hupp, *J. Am. Chem. Soc.*, 2011, **133**, 5652–5655.

100 Yakovenko, A. A.; Reibenspies, J. H.; Bhuvanesh, N.; Zhou, H.-C. Generation and Applications of Structure Envelopes for Porous Metal–Organic Frameworks. *J Appl. Crystallogr.,* 2013, **46** (2), 346–353.

101 F. Gándara and T. D. Bennett, *IUCrJ*, 2014, **1**, 563–570.

102 S. Øien-Ødegaard, G. C. Shearer, D. S. Wragg and K. P. Lillerud, *Chem. Soc. Rev.*, 2017, **46**, 4867–4876.

103 Bloch, W. M.; Burgun, A.; Coghlan, C. J.; Lee, R.; Coote, M. L.; Doonan, C. J.; Sumby, C. J. Capturing Snapshots of Post-Synthetic Metallation Chemistry in Metal–Organic Frameworks. *Nature Chem.,* 2014, **6** (10), 906–912.

104 H. de Aguiar Bicalho, P. R. Donnarumma, V. Quezada-Novoa, H. M. Titi and A. J. Howarth, , DOI:10.26434/chemrxiv.14498208.v1.

105 S. Lee, E. A. Kapustin and O. M. Yaghi, *Science*, 2016, **353**, 808–811.

106 C. X. Weichenberger, P. V. Afonine, K. Kantardjieff and B. Rupp, *Acta Crystallogr D Biol Crystallogr*, 2015, **71**, 1023–1038.

107 N. C. Burtch, H. Jasuja and K. S. Walton, *Chem. Rev.*, 2014, **114**, 10575–10612.

108 Z. Akimbekov, D. Wu, C. K. Brozek, M. Dincă and A. Navrotsky, *Phys. Chem. Chem. Phys.*, 2015, **18**, 1158–1162.

109 A. L. Spek, *Acta Crystallogr C Struct Chem*, 2015, **71**, 9–18.

110 Thommes, M.; Kaneko, K.; Neimark, A. V.; Olivier, J. P.; Rodriguez-Reinoso, F.; Rouquerol, J.; Sing, K. S. W. *Pure Appl. Chem.,* 2015, **87** (9–10), 1051–1069.

111 Fang, Q.-R.; Makal, T. A.; Young, M. D.; Zhou, H.-C. *Comment. Inorg. Chem.,* 2010, **31** (5–6), 165–195.

112 Y.-S. Bae, A. Ö. Yazaydın and R. Q. Snurr, *Langmuir*, 2010, **26**, 5475–5483.

113 D. A. Gómez-Gualdrón, P. Z. Moghadam, J. T. Hupp, O. K. Farha and R. Q. Snurr, *J. Am. Chem. Soc.*, 2016, **138**, 215–224.

114 S. Brunauer, P. H. Emmett and E. Teller, *J. Am. Chem. Soc.*, 1938, **60**, 309–319.

115 I. Langmuir, *J. Am. Chem. Soc.*, 1918, **40**, 1361–1403.

116 J. P. Olivier, *Carbon*, 1998, **36**, 1469–1472.

117 G. Kupgan, T. P. Liyana-Arachchi and C. M. Colina, *Langmuir*, 2017, **33**, 11138–11145.

118 V. N. Vukotic and S. J. Loeb, *Chem. Eur. J.*, 2010, **16**, 13630–13637.

119 Wharmby, M. T.; Henke, S.; Bennett, T. D.; Bajpe, S. R.; Schwedler, I.; Thompson, S. P.; Gozzo, F.; Simoncic, P.; Mellot-Draznieks, C.; Tao, H.; Yue, Y.; Cheetham, A. K.. *Angew. Chem. Int. Ed.,* 2015, **54** (22), 6447–6451.

120 Lázaro, I. A. *Eur. J. Inorg. Chem.,* 2020, **2020** (45), 4284–4294.

121 T. C. Wang, N. A. Vermeulen, I. S. Kim, A. B. F. Martinson, J. F. Stoddart, J. T. Hupp and O. K. Farha, *Nature Protocols*, 2016, **11**, 149–162.

122 W. J. Rieter, K. M. Pott, K. M. L. Taylor and W. Lin, *J. Am. Chem. Soc.*, 2008, **130**, 11584–11585.

123 R. C. Huxford-Phillips, S. R. Russell, D. Liu and W. Lin, *RSC Adv.*, 2013, **3**, 14438–14443.

124 K. A. White, D. A. Chengelis, M. Zeller, S. J. Geib, J. Szakos, S. Petoud and N. L. Rosi, *Chem. Commun.*, 2009, 4506.

125 K. A. White, D. A. Chengelis, K. A. Gogick, J. Stehman, N. L. Rosi and S. Petoud, *J. Am. Chem. Soc.*, 2009, **131**, 18069–18071.

126 L. L. da Luz, R. Milani, J. F. Felix, I. R. B. Ribeiro, M. Talhavini, B. A. D. Neto, J. Chojnacki, M. O. Rodrigues and S. A. Júnior, *ACS Appl. Mater. Interfaces*, 2015, **7**, 27115–27123.

127 S. Pili, P. Rought, D. I. Kolokolov, L. Lin, I. da Silva, Y. Cheng, C. Marsh, I. P. Silverwood, V. García Sakai, M. Li, J. J. Titman, L. Knight, L. L. Daemen, A. J. Ramirez-Cuesta, C. C. Tang, A. G. Stepanov, S. Yang and M. Schröder, *Chem. Mater.*, 2018, **30**, 7593–7602.

128 L. H. G. Kalinke, D. Cangussu, M. Mon, R. Bruno, E. Tiburcio, F. Lloret, D. Armentano, E. Pardo and J. Ferrando-Soria, *Inorg. Chem.*, 2019, **58**, 14498–14506.

129 Faust, T. *Nature Chem.,* 2016, **8** (11), 990–991.

130 Frameworks for Commercial Success. *Nature Chem.,* 2016, **8** (11), 987–987.

131 Hisashi Yamamoto and Kazuaki Ishihara, *Acid Catalysis in Modern Organic Synthesis*, Wiley-VCH, 1st edn., 2008.

132 N. N. Makhmudiyarova, I. R. Ishmukhametova, T. V. Tyumkina, A. G. Ibragimov and U. M. Dzhemilev, *Tetrahedron Lett.*, 2018, **59**, 3161–3164.

133 C. J. Barger, A. Motta, V. L. Weidner, T. L. Lohr and T. J. Marks, *ACS Catal.*, 2019, **9**, 9015–9024.

134 Wang, T.; Glasper, J. A.; Shanks, B. H. *Appl. Catal. A Gen.,* 2015, **498**, 214–221.

135 P. Ye, Y. Shao, X. Ye, F. Zhang, R. Li, J. Sun, B. Xu and J. Chen, *Org. Lett.*, 2020, **22**, 1306–1310.

136 J. H. Walrod II and D. A. Atwood, in *Encyclopedia of Inorganic and Bioinorganic Chemistry*, American Cancer Society, 2012.

137 M. Rimoldi, A. J. Howarth, M. R. DeStefano, L. Lin, S. Goswami, P. Li, J. T. Hupp and O. K. Farha, *ACS Catal.*, 2017, **7**, 997–1014.

138 Beyzavi, M. H.; Stephenson, C. J.; Liu, Y.; Karagiaridi, O.; Hupp, J. T.; Farha, O. K. *Front. Ener. Res.,* 2015, **2**, 63.

139 T.-Q. Song, J. Dong, A.-F. Yang, X.-J. Che, H.-L. Gao, J.-Z. Cui and B. Zhao, *Inorg. Chem.*, 2018, **57**, 3144–3150.

140 H. T. D. Nguyen, Y. B. N. Tran, H. N. Nguyen, T. C. Nguyen, F. Gándara and P. T. K. Nguyen, *Inorg. Chem.*, 2018, **57**, 13772–13782.

141 H. Xu, B. Zhai, C.-S. Cao and B. Zhao, *Inorg. Chem.*, 2016, **55**, 9671–9676.

142 Ugale, B.; Dhankhar, S. S.; Nagaraja, C. M. *Cryst. Growth Des.,* 2018, **18** (4), 2432–2440.

143 O. R. Evans, H. L. Ngo and W. Lin, *J. Am. Chem. Soc.*, 2001, **123**, 10395–10396.

144 Batista, P. K.; Alves, D. J. M.; Rodrigues, M. O.; Sá, G. F. de; Junior, S. A.; Vale, J. A. *J. Mol. Catal. A Chem.,* 2013, **379**, 68–71.

145 R. F. D'Vries, G. E. Gomez, J. H. Hodak, G. J. A. A. Soler-Illia and J. Ellena, *Dalton Trans.*, 2016, **45**, 646–656.

146 Karmakar, A.; Hazra, S.; Guedes da Silva, M. F. C.; Paul, A.; Pombeiro, A. J. L.. *CrystEngComm.,* 2016, **18** (8), 1337–1349.

147 G. E. Gomez, A. M. Kaczmarek, R. Van Deun, E. V. Brusau, G. E. Narda, D. Vega, M. Iglesias, E. Gutierrez-Puebla and M. Á. Monge, *Eur. J. Inorg. Chem.*, 2016, 1577–1588.

148 F. Gándara, E. G. Puebla, M. Iglesias, D. M. Proserpio, N. Snejko and M. Á. Monge, *Chem. Mater.*, 2009, **21**, 655–661.

149 F. Gándara, E. Gutiérrez-Puebla, M. Iglesias, N. Snejko and M. Á. Monge, *Cryst. Growth Des.*, 2010, **10**, 128–134.

150 F. Gándara, A. García-Cortés, C. Cascales, B. Gómez-Lor, E. Gutiérrez-Puebla, M. Iglesias, A. Monge and N. Snejko, *Inorg. Chem.*, 2007, **46**, 3475–3484.

151 Vitorino, M. J.; Devic, T.; Tromp, M.; Férey, G.; Visseaux, M. *Macromol. Chem. Phys.,* 2009, **210** (22), 1923–1932.

152 Ren, Y.; Lu, J.; Jiang, O.; Cheng, X.; Chen, J. *Chinese J. Catal.,* 2015, **36** (11), 1949–1956.

153 X. Wang, X. Zhang, P. Li, K. Otake, Y. Cui, J. Lyu, M. D. Krzyaniak, Y. Zhang, Z. Li, J. Liu, C. T. Buru, T. Islamoglu, M. R. Wasielewski, Z. Li and O. K. Farha, *J. Am. Chem. Soc.*, 2019, **141**, 8306–8314.

154 P. Horcajada, C. Serre, G. Maurin, N. A. Ramsahye, F. Balas, M. Vallet-Regí, M. Sebban, F. Taulelle and G. Férey, *J. Am. Chem. Soc.*, 2008, **130**, 6774–6780.

155 Y. Cui, B. Li, H. He, W. Zhou, B. Chen and G. Qian, *Acc. Chem. Res.*, 2016, **49**, 483–493.

156 H. Furukawa, F. Gándara, Y.-B. Zhang, J. Jiang, W. L. Queen, M. R. Hudson and O. M. Yaghi, *J. Am. Chem. Soc.*, 2014, **136**, 4369–4381.

157 He, Y.; Furukawa, H.; Wu, C.; O'Keeffe, M.; Chen, B. *CrystEngComm.,* 2013, **15** (45), 9328–9331.

158 D. T. de Lill and C. L. Cahill, *Chem. Commun.*, 2006, 4946–4948.

159 F. Serpaggi and G. Férey, *J. Mater. Chem.*, 1998, **8**, 2737–2741.

160 V. Kiritsis, A. Michaelides, S. Skoulika, S. Golhen and L. Ouahab, *Inorg. Chem.*, 1998, **37**, 3407–3410.

161 G. M. Sheldrick, *Acta Cryst C*, 2015, **71**, 3–8.

162 G. M. Sheldrick, *Acta Cryst A*, 2015, **71**, 3–8.

163 R. Luebke, Y. Belmabkhout, Ł. J. Weseliński, A. J. Cairns, M. Alkordi, G. Norton, Ł. Wojtas, K. Adil and M. Eddaoudi, *Chem. Sci.*, 2015, **6**, 4095–4102.

164 A. H. Assen, Y. Belmabkhout, K. Adil, P. M. Bhatt, D.-X. Xue, H. Jiang and M. Eddaoudi, *Angew. Chem. Int. Ed.*, 2015, **54**, 14353–14358.

165 R. A. Dodson, A. P. Kalenak and A. J. Matzger, *J. Am. Chem. Soc.*, 2020, **142**, 20806–20813.

166 Basma, N.; Cullen, P. L.; Clancy, A. J.; Shaffer, M. S. P.; Skipper, N. T.; Headen, T. F.; Howard, C. A. *Mol. Phys.,* 2019, **117** (22), 3353–3363.

167 B. Shan, S. M. McIntyre, M. R. Armstrong, Y. Shen and B. Mu, *Ind. Eng. Chem. Res.*, 2018, **57**, 14233–14241.

168 H.-C. "Joe" Zhou and S. Kitagawa, *Chem. Soc. Rev.*, 2014, **43**, 5415–5418.

169 J. Fonseca, T. Gong, L. Jiao and H.-L. Jiang, *J. Mater. Chem. A*, 2021, **9**, 10562–10611.

170 S. Jakobsen, D. Gianolio, D. S. Wragg, M. H. Nilsen, H. Emerich, S. Bordiga, C. Lamberti, U. Olsbye, M. Tilset and K. P. Lillerud, *Phys. Rev. B*, 2012, **86**, 125429.

171 M. J. Van Vleet, T. Weng, X. Li and J. R. Schmidt, *Chem. Rev.*, 2018, **118**, 3681–3721.

172 R. P. Donnarumma, S. Frojmovic, P. Marino, H. de A. Bicalho, H. M. Titi and A. J. Howarth, *Chem. Commun.*, 2021.

173 C. Daiguebonne, N. Kerbellec, O. Guillou, J.-C. Bünzli, F. Gumy, L. Catala, T. Mallah, N. Audebrand, Y. Gérault, K. Bernot and G. Calvez, Structural and Luminescent Properties of Micro- and Nanosized Particles of Lanthanide Terephthalate Coordination Polymers.

174 J. Jacobsen, A. Ienco, R. D'Amato, F. Costantino and N. Stock, *Dalton Trans.*, 2020, **49**, 16551–16586.

175 Janicki, R.; Mondry, A.; Starynowicz, P. *Coord. Chem. Rev.,* 2017, **340**, 98–133.

Appendix

Table A.1. Crystallographic data for Tm-UiO-66 synthesised from DMA and HCl.

Empirical formula	$C_{24}H_{12}O_{16}Tm_3$
Formula weight	1062.13
Temperature/K	253(2)
Crystal system	Cubic
Space group	$Fm\bar{3}m$
a/Å	21.2553(16)
b/Å	21.2553(16)
c/Å	21.2553(16)
$\alpha/°$	90
$\beta/°$	90
$\gamma/°$	90
Volume/ Å^3	9603(2)
Z	8
ρ_{calc}/g/cm^3	1.471
μ/mm^{-1}	10.408
F(000)	3928.0
2θ range for data collection/°	7.204 to 144.87
Index ranges	-26<=h<=26 -26<=k<=26 -26<=l<=26
Reflections collected	43503
Independent reflections	539 [Rint = 0.1137, Rsigma = 0.0208]
Data/restraints/parameters	539/12/27
Goodness-of-fit on F^2	1.173
Final R indexes [I>=2σ (I)]	$R_1 = 0.0369$, $wR_2 = 0.0950$
Final R indexes [all data]	$R_1 = 0.0433$, $wR_2 = 0.1065$
Largest diff. peak/hole / e Å^{-3}	1.09/-1.08

184 e$^-$ were squeezed from the structure due to an impossibility to solve the molecules in the pores due to the high level of disorder. To this point the structure was solved yielding the following formula: $Tm_3(OH)_4(BDC)_3$. This framework is anionic, and its charge needs to be countered with a counterion. $[CH_3)_2NH_2]^+$ is the only possible present counterion needed to balance the charge so, 26 e$^-$ have to belong to it. The remaining 158 e$^-$ are assigned to 3 DMA molecules (48e$^-$ each) and 1.5 H$_2$O molecules (10 e$^-$ each). The final formula for this compound ends would then be $[(CH_3)_2NH_2]_1[Tm_3(OH)_4(BDC)_3]\cdot(DMA)_3\cdot(H_2O)_{1.5}$.
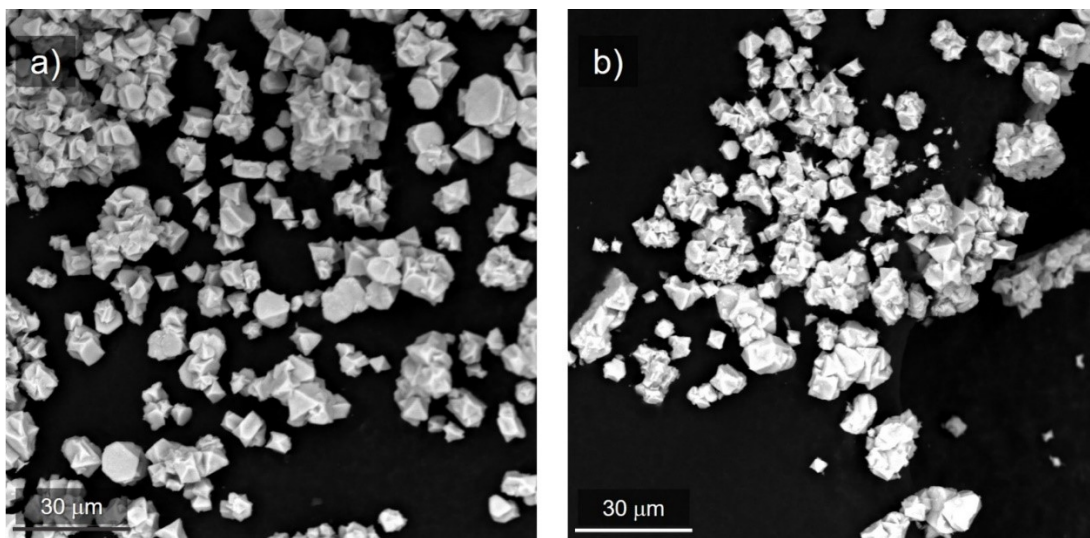
Figure A.1. SEM of (a) Yb-UiO-66 and (b) Er-UiO-66. Octahedral shapes can be distinguished in the images.

Table A.2. Crystallographic data for RE-UiO-66 synthesised from DMA and HCOOH.

Identification code	Y-UiO-66	Eu-UiO-66	Gd-UiO-66	Tb-UiO-66
Empirical formula	$C_{16}H_8O_{10.67}Y_2$	$C_{12}H_6Eu_{1.5}O_{8.38}$	$C_{24}H_{12}Gd_3O_{16}$	$C_{12}H_6O_{8.57}Tb_{1.5}$
Formula weight	548.71	512.13	1028.09	525.68
Temperature/K	273.15	273.15	298(2)	298.15
Crystal system	cubic	cubic	cubic	cubic
Space group	Fm-3m	Fm-3m	Fm-3m	Fm-3m
a/Å	21.4346(3)	21.6291(9)	21.6515(5)	21.5993(3)
b/Å	21.4346(3)	21.6291(9)	21.6515(5)	21.5993(3)
c/Å	21.4346(3)	21.6291(9)	21.6515(5)	21.5993(3)
α/°	90	90	90	90
β/°	90	90	90	90
γ/°	90	90	90	90
Volume/Å^3	9848.0(4)	10118.5(13)	10150.0(7)	10076.7(4)
Z	12	15.99936	8	15.99936
ρcalcg/cm^3	1.11	1.345	1.346	1.386
μ/mm^{-1}	5.031	26.665	25.382	20.759
F(000)	3208	3832	3808	3905
Crystal size/mm^3	0.1 × 0.1 × 0.1	0.12 × 0.118 × 0.062	0.144 × 0.112 × 0.109	0.092 × 0.091 × 0.073
Radiation	CuKα (λ = 1.54178)	CuKα (λ = 1.54178)	CuKα (λ = 1.54178)	CuKα (λ = 1.54178)
2θ range for data collection/°	8.25 to 143.926	7.078 to 140.886	7.072 to 144.618	11.588 to 144.48
Index ranges	-21 ≤ h ≤ 26, -25 ≤ k ≤ 26, -26 ≤ l ≤ 26	-23 ≤ h ≤ 25, -16 ≤ k ≤ 26, -25 ≤ l ≤ 21	-26 ≤ h ≤ 26, -23 ≤ k ≤ 26, -26 ≤ l ≤ 26	-26 ≤ h ≤ 20, -23 ≤ k ≤ 26, -22 ≤ l ≤ 19
Reflections collected	14239	6412	14660	6544
Independent reflections	550 [R_{int} = 0.1082, R_{sigma}= 0.0360]	552 [R_{int} = 0.0840, R_{sigma} = 0.0571]	564 [R_{int} = 0.2013, R_{sigma} = 0.0477]	557 [R_{int} = 0.0547, R_{sigma} = 0.0254]
Data/restraints/parameters	550/0/27	552/9/30	564/0/27	557/0/27
Goodness-of-fit on F_2	1.28	1.072	1.067	1.09
Final R indexes [I>=2σ (I)]	R_1 = 0.0561, wR_2 = 0.1982	R_1 = 0.0959, wR_2 = 0.2316	R_1 = 0.0495, wR_2 = 0.1408	R_1 = 0.0386, wR_2 = 0.1053
Final R indexes [all data]	R_1 = 0.0583, wR_2 = 0.2000	R_1 = 0.1013, wR_2 = 0.2363	R_1 = 0.0586, wR_2 = 0.1474	R_1 = 0.0442, wR_2 = 0.1147
Largest diff. peak/hole / e Å^{-3}	1.34/-0.97	2.63/-1.86	1.79/-0.68	1.06/-0.80

Identification code	Ho-UiO-66	Er-UiO-66	Tm-UiO-66	Yb-UiO-66
Empirical formula	$C_{12}H_{1.5}Ho_{1.5}O_8$	$C_{16}H_8Er_2O_{10.67}$	$C_{12}H_6O_{8.37}Tm_{1.5}$	$C_{16}H_8O_{10.67}Yb_2$
Formula weight	521.05	705.41	537.53	716.97
Temperature/K	296.15	273.15	273.15	273.15
Crystal system	cubic	cubic	cubic	cubic
Space group	Fm-3m	Fm-3m	Fm-3m	Fm-3m
a/Å	21.4685(3)	21.3828(6)	21.310(4)	21.2388(16)
b/Å	21.4685(3)	21.3828(6)	21.310(4)	21.2388(16)
c/Å	21.4685(3)	21.3828(6)	21.310(4)	21.2388(16)
$\alpha/°$	90	90	90	90
$\beta/°$	90	90	90	90
$\gamma/°$	90	90	90	90
Volume/Å^3	9894.8(4)	9776.7(8)	9677(5)	9581(2)
Z	15.99936	12	15.99936	12
ρcalcg/cm^3	1.399	1.438	1.476	1.491
μ/mm^{-1}	8.984	9.584	10.346	10.858
F(000)	3808	3904	3976	3952
Crystal size/mm^3	0.106 × 0.1 × 0.086	0.076 × 0.073 × 0.021	0.289 × 0.094 × 0.079	0.095 × 0.065 × 0.051
Radiation	CuKα (λ = 1.54178)	CuKα (λ = 1.54178)	CuKα (λ = 1.54178)	CuKα (λ = 1.54178)
2θ range for data collection/°	7.132 to 136.058	8.27 to 144.79	7.184 to 140.054	7.208 to 139.24
Index ranges	-23 ≤ h ≤ 19, -25 ≤ k ≤ 24, -23 ≤ l ≤ 25	-25 ≤ h ≤ 26, -25 ≤ k ≤ 26, -26 ≤ l ≤ 26	-16 ≤ h ≤ 13, -15 ≤ k ≤ 25, -21 ≤ l ≤ 24	-25 ≤ h ≤ 8, -22 ≤ k ≤ 16, -17 ≤ l ≤ 19
Reflections collected	7355	41256	2474	3025
Independent reflections	514 [Rint=0.0566, Rsigma=0.0262]	549 [Rint=0.0659, Rsigma=0.0131]	517 [Rint=0.1142, Rsigma= 0.0732]	506 [Rint =0.0981, Rsigma=0.0764]
Data/restraints/parameters	514/9/27	549/0/27	517/6/28	506/6/27
Goodness-of-fit on F$_2$	1.085	1.038	0.933	1.01
Final R indexes [I>=2σ (I)]	R_1 = 0.0415, wR_2 = 0.1338	R_1 = 0.0279, wR_2 = 0.0809	R_1 = 0.0370, wR_2 = 0.0801	R_1 = 0.0598, wR_2 = 0.1501
Final R indexes [all data]	R_1 = 0.0477, wR_2 = 0.1378	R_1 = 0.0285, wR_2 = 0.0816	R_1 = 0.0489, wR_2 = 0.0853	R_1 = 0.0687, wR_2 = 0.1551
Largest diff. peak/hole / e Å^{-3}	1.68/-1.10	1.36/-0.58	1.10/-1.31	1.53/-1.40